Engineering Geology 327 (2023) 107315

Contents lists available at ScienceDirect

Engineering Geology

journal homepage: www.elsevier.com/locate/enggeo

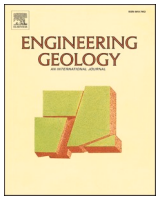

Preliminary documentation of coseismic ground failure triggered by the February 6, 2023 Türkiye earthquake sequence

Tolga Görüm [a,*], Hakan Tanyas [b,*], Furkan Karabacak [a], Abdüssamet Yılmaz [a], Serkan Girgin [b], Kate E. Allstadt [c], M. Lütfi Süzen [d], Paula Burgi [c]

[a] Eurasia Institute of Earth Sciences, Istanbul Technical University, Istanbul, Türkiye
[b] University of Twente, Faculty of Geo-Information Science and Earth Observation (ITC), Enschede, the Netherlands
[c] U.S. Geological Survey, Geologic Hazards Science Center, Golden, CO, USA
[d] Middle East Technical University, Geological Engineering Department, Ankara, Türkiye

ARTICLE INFO

Keywords:
Landslides
Earthquake
Rock fall
Bedrock rotational slide
Translational slides
Lateral spread

ABSTRACT

The devastating Kahramanmaraş earthquake sequence occurred on February 6, 2023. Two main events, M_w 7.8 and M_w 7.5 occurred 9 hours apart, affected 11 cities in Turkey, and subjected an area of ~90,000 km^2 to shaking levels known to trigger landslides (peak ground acceleration > 0.08 g). Extensive landsliding was expected given the hilly terrain affected by this significant ground shaking—about 15% of the topography is steeper than 20°—but was not initially apparent in early satellite imagery, mostly because of obscuring snow that fell just after the earthquakes. However, after a more detailed investigation using high-resolution satellite images, aerial photos, and a field survey, we confirmed that this earthquake sequence did, indeed, trigger numerous landslides. In this study, we present those findings and provide a preliminary characterization of the spatial distribution, general characteristics, and dominant types of landslides and hillslope deformation triggered by the earthquake sequence. We mapped 3673 coseismic landslides, mostly concentrated in the northern half of the impacted area. Rock falls are the most abundant landslide type, but bedrock rotational landslides, translational slides and lateral spreads are also numerous. Surface rupture through mountainous terrain caused several large, and in some cases fatal, landslides. Incipient landslides and ground cracks are also widespread, especially in the north. Lithology, spatial variability of ground shaking, and topographic relief appear to be the main variables controlling the spatial distribution of coseismic landslides. There are few detailed studies of earthquake-triggered landslides in arid and semi-arid regions such as this one, nor for such complex earthquake sequences. Therefore, this contribution provides valuable information for future hazard and modeling efforts in arid and semi-arid regions.

1. Introduction

Türkiye is located within the Alpine-Himalayan mountain belt and is one of the most actively deforming regions in the world (Bozkurt and Mittwede, 2001). In the last three decades, the country was affected by several strong earthquakes including the 1999 Mw 7.6 Izmit, 1999 Mw 7.2 Düzce, 2011 Mw 7.1 Van, 2020 Mw 6.8 Elazığ and 2020 Mw 7.0 İzmir earthquakes. And yet, earthquake-induced landslides (EQILs) in Türkiye rarely have been investigated or documented. So far, EQIL inventories are available only for the 2011 Van (Görüm, 2016) and the 2020 Elazığ (Karakas et al., 2021) earthquakes. As a result, compared to other mountainous landscapes experiencing strong earthquakes triggering tens of thousands of EQILs (e.g., Gorum et al., 2013; Harp and Jibson, 1996; Roback et al., 2018; Tanyaş et al., 2022; Xu et al., 2014; Zhao, 2021), the characteristics of historical EQILs have been poorly examined in Türkiye.

On the early morning of 6 February 2023 at 04.17 UTC + 3, a strong earthquake (the Pazarcık earthquake) struck southeastern Türkiye and northwestern Syria (Fig. 1). It occurred along the left-lateral East Anatolian Fault Zone. The magnitude of the earthquake was estimated as M_w 7.7 by the Kandilli Observatory and Earthquake Research Institute (KOERI) and M_w 7.8 by the U.S. Geological Survey (USGS). This was the strongest earthquake recorded in this region since the Mw 7.81938 Erzincan earthquake. Nine hours after this event, another strong earthquake (the Ekinözü earthquake), estimated as Mw 7.6 by KOERI and Mw 7.5 by the USGS occurred approximately 90 km north of the

* Corresponding authors.
E-mail addresses: tgorum@itu.edu.tr (T. Görüm), h.tanyas@utwente.nl (H. Tanyas).

https://doi.org/10.1016/j.enggeo.2023.107315
Received 10 June 2023; Received in revised form 22 September 2023; Accepted 4 October 2023
Available online 13 October 2023

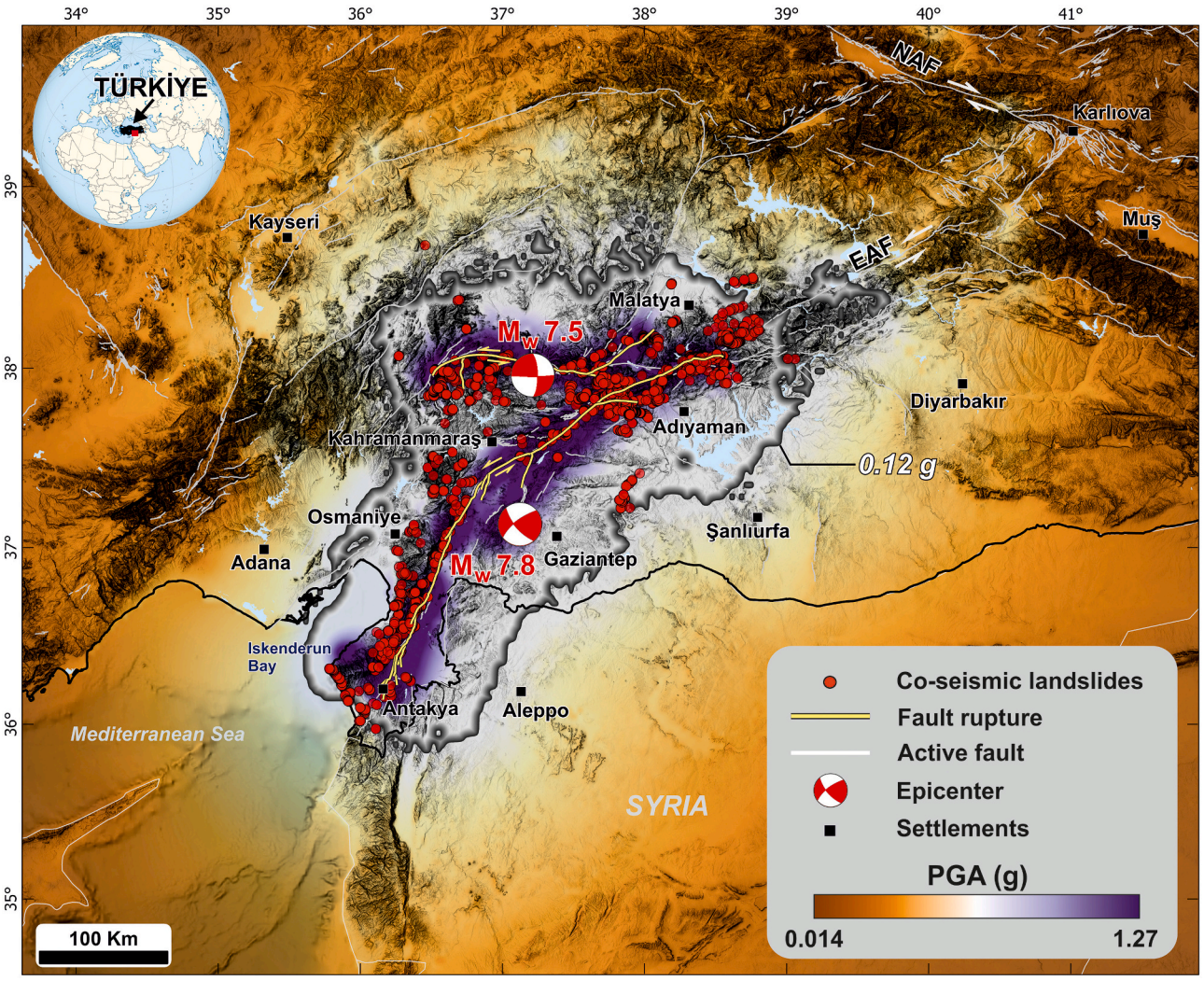

Fig. 1. Spatial distribution of coseismic landslides overlain by the two main earthquake epicenters (U.S. Geological Survey, 2023a, 2023b) fault rupture (yellow, Reitman et al., 2023) and the USGS composite peak ground acceleration (PGA) map representing the maximum PGA recorded at each location for all quakes of magnitude 5.5 and larger from the sequence (Goldberg et al., 2023). Major active faults (Emre et al., 2013) are indicated by white lines. EAF: Eastern Anatolian Fault, NAF: North Anatolian Fault. The 0.12 g PGA contour is shown with a dark gray line. (For interpretation of the references to colour in this figure legend, the reader is referred to the web version of this article.)

mainshock's epicenter. Together, these two earthquakes are named the Kahramanmaraş earthquake sequence in reference to the City of Kahramanmaraş, which is located near the center of the impacted area (Fig. 1).

This was the strongest historical earthquake doublet of magnitudes above 7.5 ever recorded in this region, and the consequences were catastrophic. As of March 30, 2023, the Disaster and Emergency Management Presidency (AFAD) of Türkiye reported 50,096 fatalities, 107,204 injuries, and 3 million people displaced. An area of ~90,000 km^2 experienced peak ground accelerations (PGA) of 0.08 g or greater, and >15 million inhabitants were significantly affected by the earthquake sequence. Here, and throughout the rest of the paper, we use PGA estimates from the USGS composite ShakeMap for the sequence (Goldberg et al., 2023; Wald et al., 2023), which reports the maximum PGA value recorded at each grid for either mainshock and for any aftershocks >M_w 5.5.

The earthquake doublet affected mountainous terrain and thus the near-real-time USGS Ground Failure (GF) product (Allstadt et al., 2022) predicted the highest possible landslide alert level (red) for both earthquakes because of an estimated extensive area exposed to landslide hazard (>100 km^2) and extensive number of people living in areas that could have produced landslides (>10,000 people) (U.S. Geological Survey, 2023a, 2023b). These estimates are based on aggregate statistics for hazard and population exposure that are computed based on geospatial probability maps output by a globally available statistical geospatial landslide model (Nowicki Jessee et al., 2018) as outlined in (Allstadt et al., 2022). The probabilistic model approach proposed by Nowicki Jessee et al. (2018) is based on a logistic regression algorithm fed by ground shaking, slope steepness, lithology, land cover type and topographic wetness index. In the resultant map, high landslide probabilities, representing predicted landslide areal coverage for the composite ShakeMap at a resolution of about ~250 m, were modeled along the west side of the fault in the south and both sides of the fault in the north, with a gap south of Kahramanmaraş (Fig. 2a).

A comparison of the USGS GF product aggregate statistics for the combined Türkiye earthquake sequence to other well-known historical landslide-triggering earthquakes (Fig. 2b) suggests that this sequence was similar but slightly higher in terms of both hazard and population exposure than the 1999 M_w 7.6 ChiChi, Taiwan and 2011 M_w 9.1 Tohoku, Japan earthquakes, and similar in hazard but far higher in terms of population exposure than the 2016 M_w 7.8 Kaikoura, New Zealand and 2002 M_w 7.9 Denali, Alaska earthquakes. However, despite

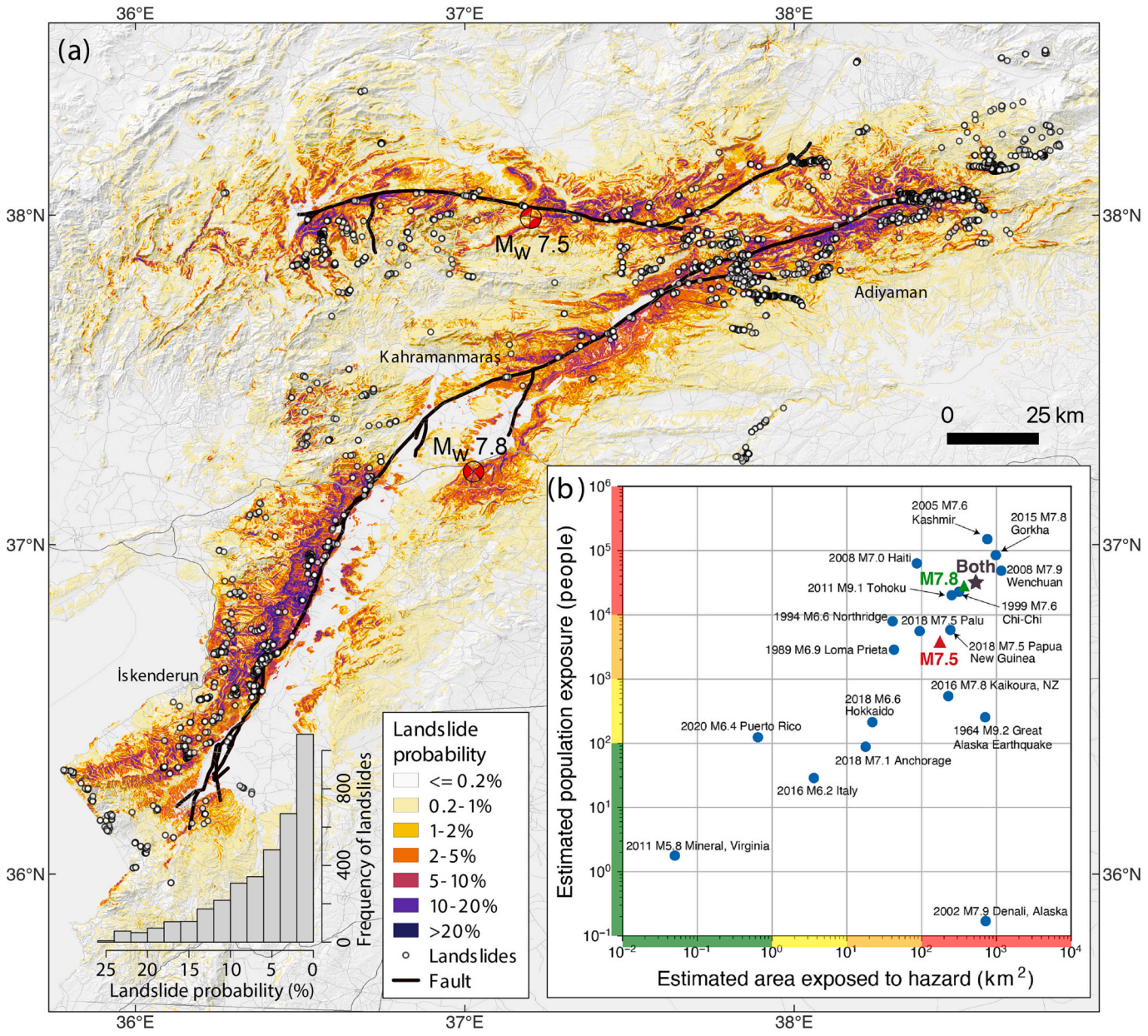

Fig. 2. USGS Ground Failure product results for the composite ShakeMap (considering both mainshocks and all aftershocks >M5.5), showing the distribution of landslide probabilities in panel (a), which represent a prediction of the proportion of the area that could be affected by landslides. Coseismic landslides mapped in this study are overlain for comparison. Panel (b) compares the aggregate statistics for area exposed to hazard and population exposure for the Mw 7.8 Pazarcık earthquake and the Mw 7.5 Ekinözü earthquake (triangles) and the composite Kahramanmaraş earthquake sequence (star, labeled "both") to other well-known historical landslide-triggering earthquakes. The four alert levels used for each aggregate statistic are delineated along the axes.

having the highest alert level, the overall estimated hazard and population exposure was substantially lower than three of the most severe landslide-triggering events on record: the 2005 M_w 7.6 Kashmir, 2015 M_w 7.8 Gorkha, and 2008 M_w 7.9 Wenchuan earthquakes. This event sequence might also be the largest historical earthquake-induced landslide event ever recorded in Türkiye because the previously documented EQIL events triggered only a few hundred landslides (Görüm, 2016; Karakas et al., 2021).

In the days immediately following the earthquake, we examined high-resolution satellite images and aerial photos to identify landslides of particular concern for human safety and to provide situational awareness to authorities. We also sought better insight into the spatial distribution of coseismic landslides. This remote campaign was supplemented a few weeks after the earthquake by field surveys. Here we present the preliminary findings of these investigations.

2. Study area

Global observations show that a coseismic landslide could be triggered in the far field with PGA values as low as 0.02–0.08 g (Jibson and Harp, 2016), but most occur at higher levels of shaking. Typically, about 90% of landslides occur where PGA exceeds 0.12 g (Tanyaş and Lombardo, 2019). Though this value can differ depending on the topographic characteristics of a given earthquake-affected area, we consider 0.12 g PGA as a good first approximation of the PGA contour likely containing most of the landslides. Therefore, all subsequent analyses in this study were conducted for the areas bounded by the 0.12 g PGA contour (Fig. 1).

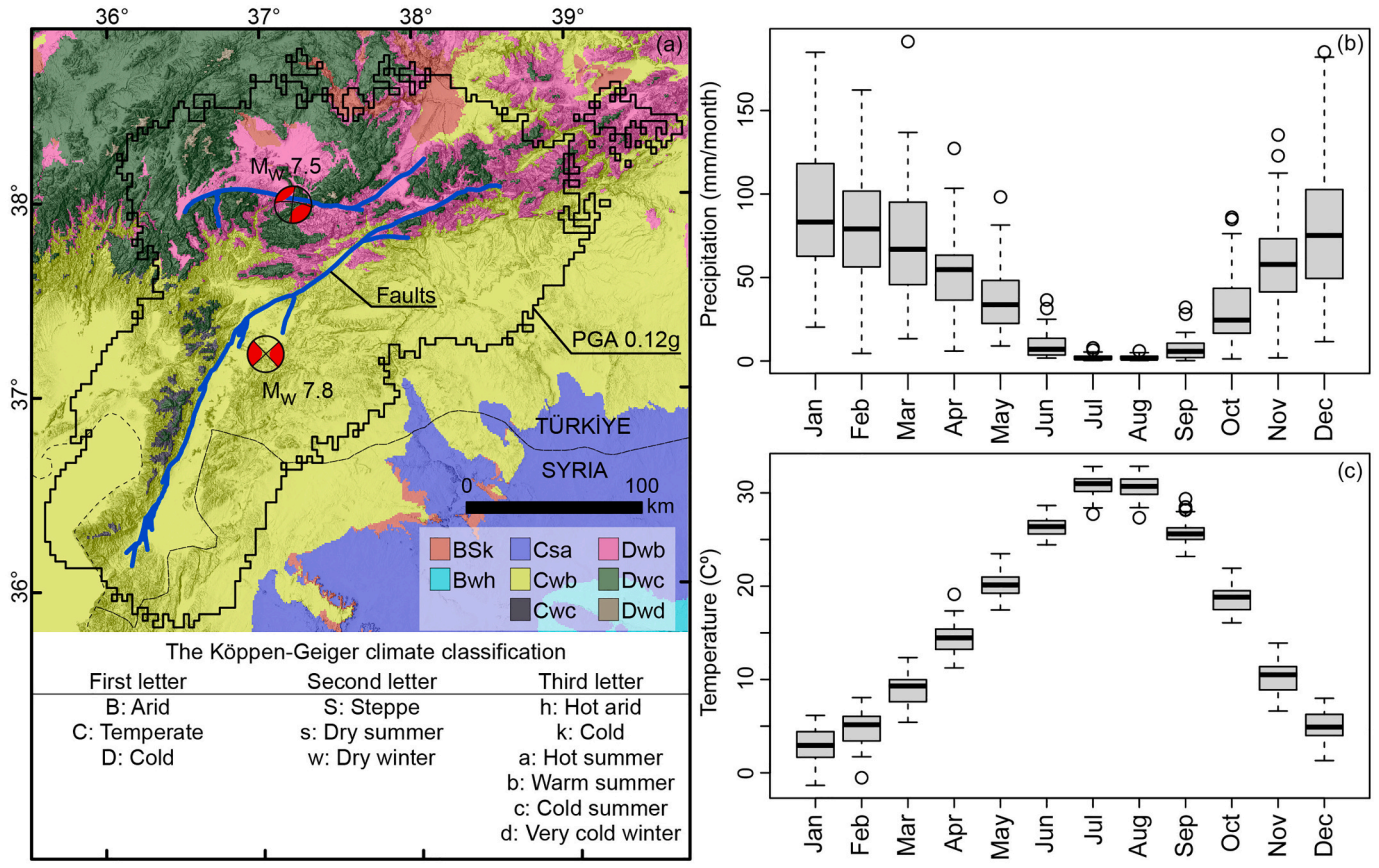

Fig. 3. Panels showing (a) climatic zones, (b) average monthly precipitation, and (c) average monthly temperature in the study area. The updated version of the Köppen-Geiger climate classification (Peel et al., 2007) is used in panel (a). MERRA-2 data produced by NASA Global Modeling and Assimilation Office (GMAO (Global Modeling and Assimilation Office), 2015) is used to generate precipitation and temperature patterns in panels (b) and (c).

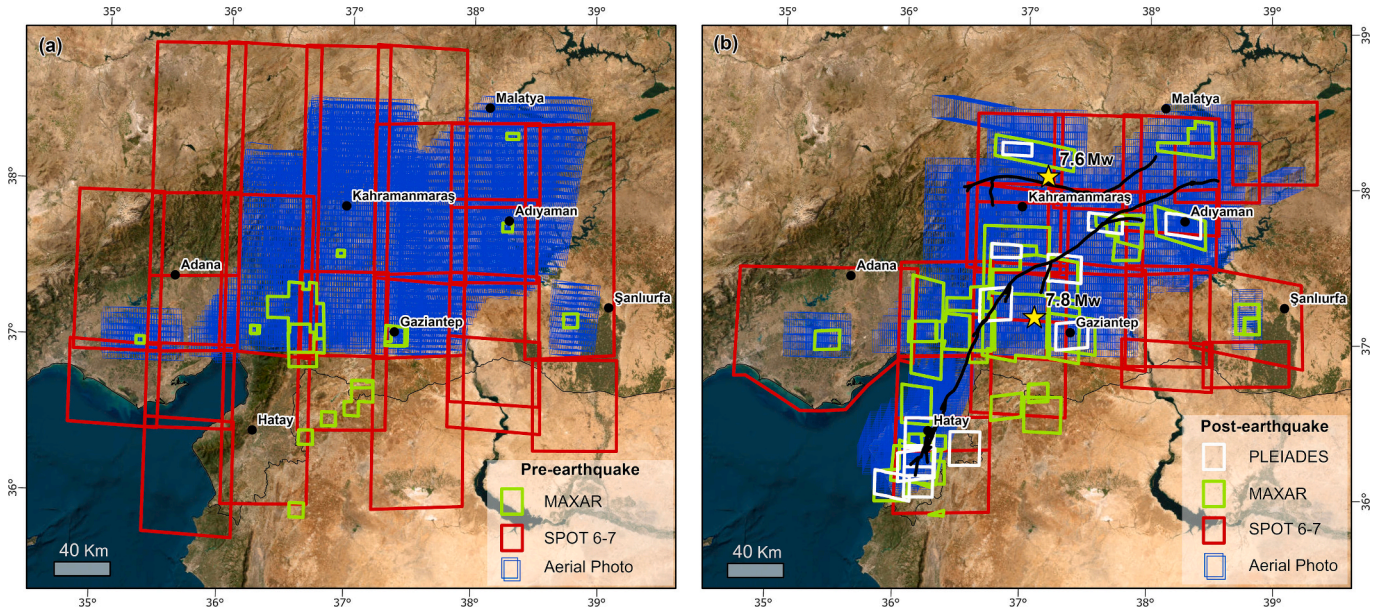

Fig. 4. Pre- (a) and post-earthquake (b) aerial photo and satellite image coverage.

2.1. Tectonic setting and characteristics of the earthquake doublet

The earthquake doublet of February 6, 2023 in Türkiye occurred in the left-lateral East Anatolian Fault (EAF) zone, one of the main intra-continental transform faults in the eastern Mediterranean region (Arpat and Şaroğlu, 1972; Duman and Emre, 2013; Şengör and Yazıcı, 2020). The EAF zone (see Fig. 1) starts at the Karlıova triple junction, where the EAF meets the right-lateral North Anatolian Fault (NAF) zone in the northeast and extends southward for about 550 km to Iskenderun Bay in the Mediterranean Sea (Duman and Emre, 2013; Herece, 2008; Köküm

Table 1
List of satellite images and aerial photos used in landslide mapping. We did not rectify any of the images, but instead relied on the rectification provided by the vendors.

Source	Spatial resolution (m)	Pre-seismic imagery			Post-seismic imagery		
		# of images	Total area (km2)	Dates	# of images	Total area (km2)	Dates
Aerial photos (HGM)	0.3	7560	43,468	06-09-2016/ 15-08-2020	5525	44,927	07-02-2023/ 21-02-2023
SPOT-6 & 7	1.5	19	106,331	03-04-2022/ 20-12-2022	20	64,641	07-02-2023/ 09-03-2023
MAXAR	0.3	18	3386	01-06-2010/ 26-01-2023	24	20,113	07-02-2023/ 28-02-2023
PLEIADES	0.5	–	–		13	5255	08-02-2023/ 01-03-2023

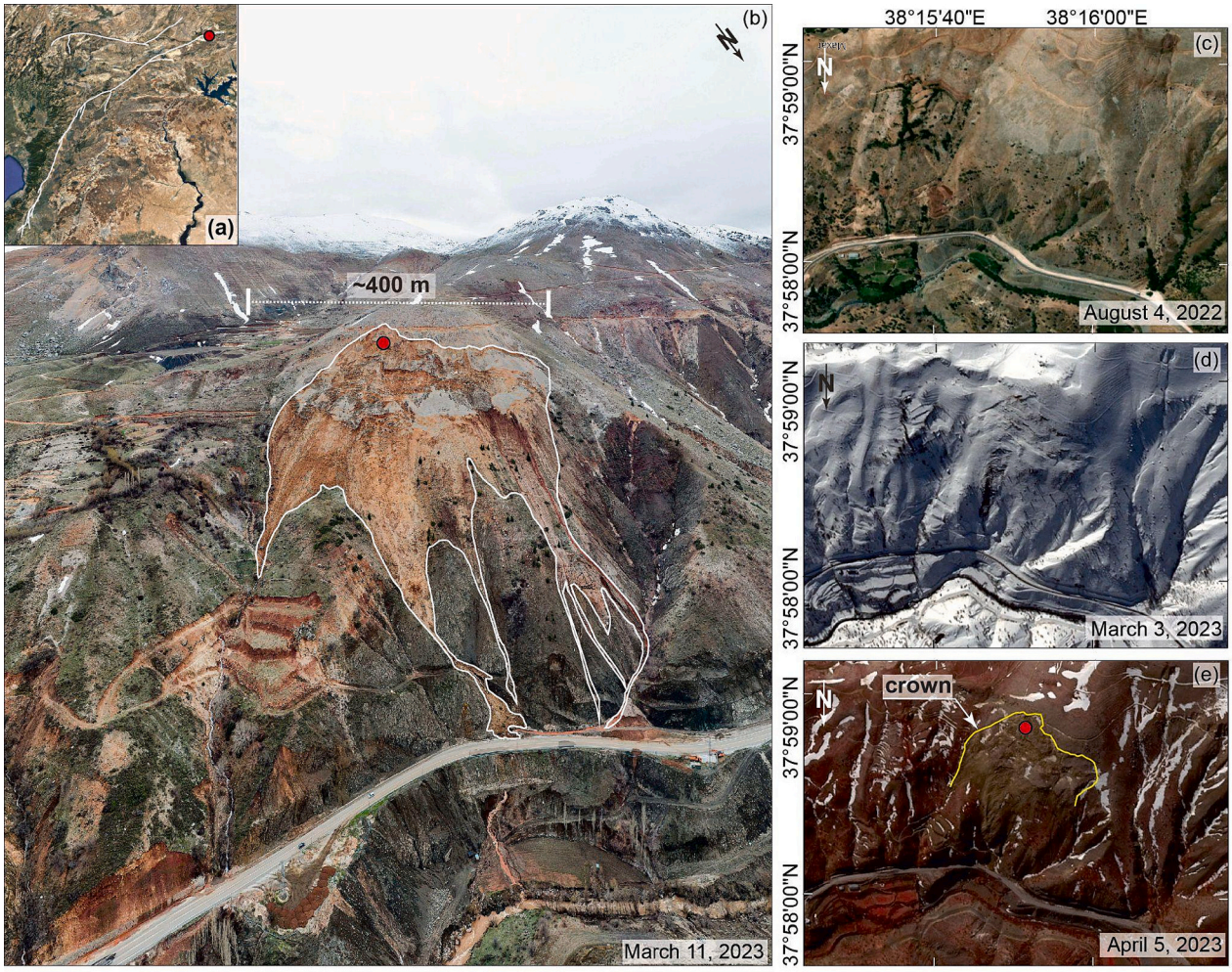

Fig. 5. Aerial and satellite images show an example of a landslide whose mapping was hampered by snow cover near Çelikhan, Adıyaman. Panel (a) shows the locus of the landslide, panel (b) shows an oblique view, acquired by UAV, of the landslide (white polygon) on 11 March 2023. Panel (c) shows this area in a pre-event satellite image (Airbus), panel (d) shows the same area covered in snow after the earthquake (3 March 2023 aerial image), and panel (e) shows the area in a SPOT-7 image collected on 5 April 2023 after the snow melted where the landslide is more clearly visible (yellow line indicates the landslide crown). The red point in panels (a) and (b) shows the landslide location used in the inventory. (For interpretation of the references to colour in this figure legend, the reader is referred to the web version of this article.)

and İnceöz, 2018; Tatar et al., 2020). The transform characteristic of this fault zone, on which many destructive historical earthquakes have occurred (Ambraseys, 2009; Ambraseys, 1989; Arpat, 1971; Arpat and Şaroğlu, 1975; Dewey et al., 1986; Kaymakci et al., 2010; McKenzie, 1976; McKenzie, 1972; Stiros, 2022; Stucchi et al., 2022; Tan et al., 2008; Tatar et al., 2020; Taymaz et al., 2021; Taymaz et al., 1991; Westaway, 2003), was first defined by Arpat and Şaroğlu (1972). The EAF consists of >15 segments having different slip rates (Herece, 2008). Relative plate motion is accommodated predominantly by left-lateral strike-slip faulting at slip rates of 10 ± 1 mm/yr in the northern strand (Reilinger et al., 2006), decreasing to 4.5 mm/yr in the south (Aktug et al., 2016).

During the February 6, 2023 earthquake sequence, surface rupture length was 270 km ± 10 km and 167 km ± 12 km for the M_w 7.8 Pazarcık earthquake (Karabacak et al., 2023) and M_w 7.5 Ekinözü earthquake (Kurcer et al., 2023), respectively. This earthquake sequence produced extremely complex rupture dynamics (Abdelmeguid et al., 2023; Mai et al., 2023; Melgar et al., 2023; Okuwaki et al., 2023; Stein et al., 2023), with maximum left-lateral displacements of 7.3 m for the Mw 7.8 Pazarcık (Karabacak et al., 2023) and 8.8 m for the Mw 7.5 Ekinözü (Kurcer et al., 2023) earthquake. Inversion of Interferometric Synthetic Aperture Radar (InSAR) and Global Positioning System (GPS) data revealed significant lateral variations of fault slip and locking depths along the central and western segments of the EAF, which

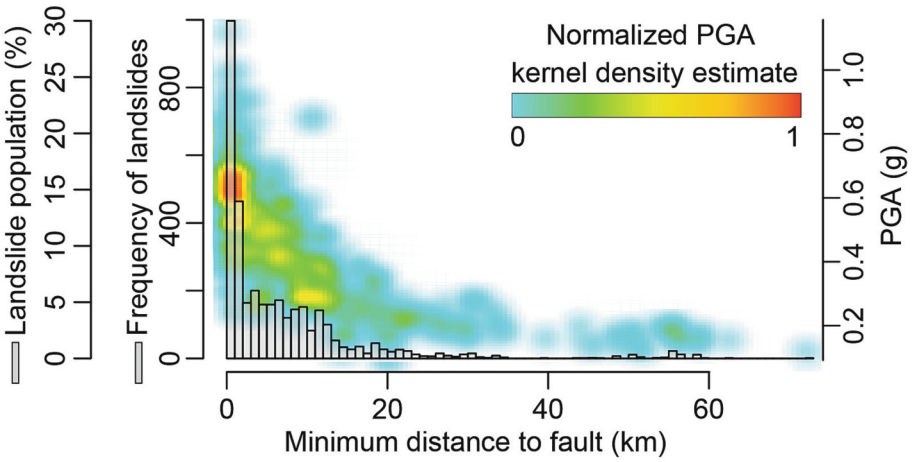

Fig. 6. Population and frequency distributions of landslides as a function of distance to the fault. The background colors show the kernel-density estimates of the PGA at landslide locations with respect to fault-rupture distance.

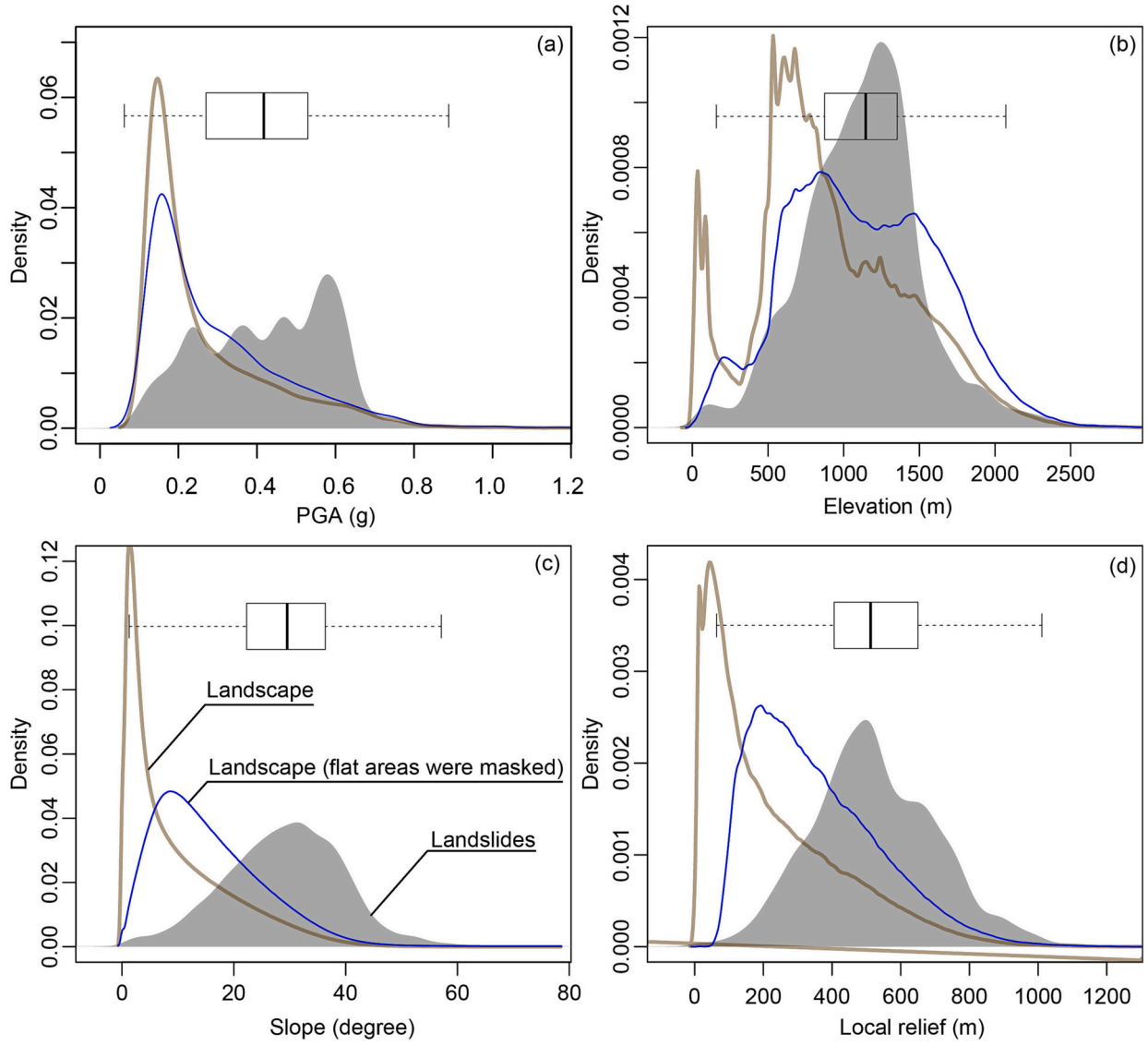

Fig. 7. Frequency distribution of (a) PGA, (b) elevation, (c) slope, and (d) local relief expressed as kernel density estimates (Sheather and Jones, 1991) for both landslide locations and the entire landscape. Landscape characteristics are shown with and without flat areas. Boxplots were generated for landslide locations.

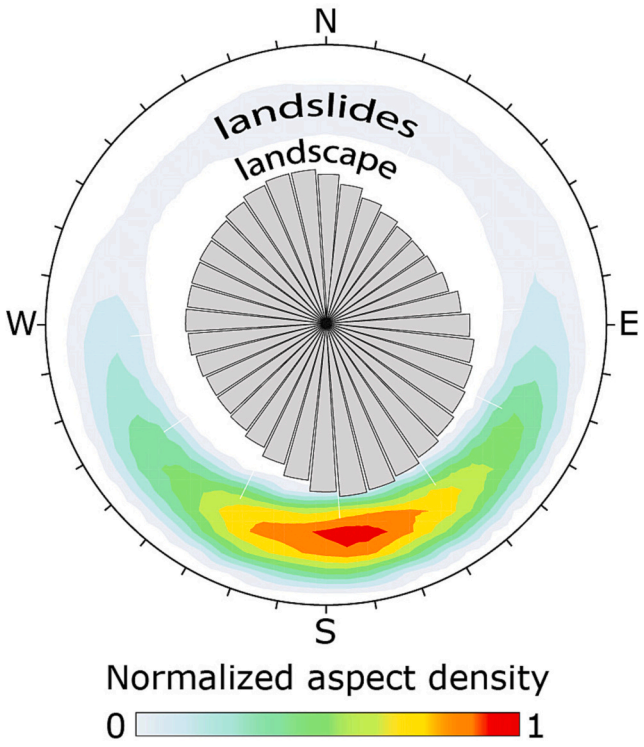

Fig. 8. Rose diagram showing the aspect distribution of coseismic landslides (contouring) and the landscape (binned rosette plot) in the examined area. (For interpretation of the references to colour in this figure legend, the reader is referred to the web version of this article.)

suggested large heterogeneity of the slip along individual fault planes (Li et al., 2023).

2.2. Climatic characteristics of the study area

The study area is located within the Mediterranean region, characterized by mild wet winters and warm to hot, dry summers (Lionello et al., 2006). However, within the area affected by the earthquake sequence, the dominant climate conditions range from cold and arid in the north, to temperate in the south (Fig. 3a). The variation is controlled mainly by the mountainous landscape becoming more prominent toward the north. Based on the updated version of the Köppen-Geiger climate classification (Peel et al., 2007), the study area includes seven climatic zones.

July and August are the driest and the hottest months; January and February have the most precipitation (Fig. 3b and c). Even in this wet season, the average precipitation is <100 mm/month.

3. Sources and methods

3.1. Landslide mapping

We followed a four-step methodology to map landslides: (i) collecting satellite images and aerial photos, (ii) identifying landslide hot spots with the collected imagery, (iii) carrying out a field survey, and (iv) mapping landslides using collected images and field observations. All landslides were mapped as points. Steps iii was conducted only for a subset of the landslides, about 20–30% of those mapped.

We collected all available satellite imagery and aerial photos showing pre- and post-seismic conditions. This included high-resolution aerial photos shared by the General Directorate of Mapping of Türkiye (Harita Genel Müdürlüğü, HGM), SPOT-6-7 (1.5 m) and MAXAR images (0.3 m) shared by MAXAR's Open Data Program and Pleiades imagery provided by AIRBUS. Overall, we examined an area of ~45,000 km^2 using aerial photos and expanded this area by visually examining 7597 pre-earthquake and 5582 post-earthquake satellite images, which were available through HGM's Geoportal (https://geoportal.harita.gov.tr/) (Fig. 4 and Table 1).

We then manually scanned these images to identify areas hosting large landslides or locations with high landslide concentrations. At this stage, we did not map individual landslides but identified landslide hot spots.

Next, we carried out a three-week field survey to visit some of the identified locations. At each site, we recorded post-seismic landscape conditions using a DJI Mavic Pro 2 unmanned aerial vehicle (UAV).

Field verification was an essential step of landslide mapping because in the early morning of February 6, the earthquake-affected area received snowfall that obscured the terrain and made interpretation of remote-sensing imagery challenging. Fig. 5 shows an example of an area where we mapped a coseismic landslide after the snow cover melted. A comparison between the first coseismic image (an aerial photo) acquired on March 3, 2023 (Fig. 5d) and its pre-seismic counterpart acquired on August 4, 2022 (Airbus satellite imagery available from Google Earth, Fig. 5c) barely shows the footprint of the landslide because of snow cover. In contrast, the SPOT-7 Image acquired on May 5, 2023, after the snow melted, shows surface deformations associated with the landslide (Fig. 5e). Local residents confirmed that the landslide was triggered by the earthquakes on February 6.

Ultimately, we re-examined the satellite and aerial imagery again, guided by our field observations, and mapped individual landslides triggered by the earthquake sequence. We manually assigned points in the approximate source areas.

3.2. Analyzing the spatial distribution of landslides

We analyzed the spatial distribution of coseismic landslides in relation to topography, geology, and ground shaking. For topography, we used a 5-m resolution digital elevation model (DEM) derived from pre-event stereo aerial photos (mostly 2019) acquired by the Turkish Command of Mapping. We used the DEM to quantify elevation, slope, local relief, and aspect of landslide locations as well as overall landscape conditions. We calculated local relief as the maximum difference in elevation within a circular moving window with a 1-km radius. To characterize the geology, we used 1:500,000 geological maps of Türkiye (MTA, 2002) and analyzed the spatial distribution of landslides over both geological units and specific rock types. To examine the spatial distribution of landslides with respect to ground shaking, we used two variables: (1) PGA from the USGS PGA map shown in Fig. 1, and (2) distance to the surface fault rupture.

Grids of estimated ground-shaking from the main earthquake shocks are commonly are used to analyze the spatial distribution of landslides (e.g., Gallen et al., 2017; Jibson et al., 2000; Parker et al., 2015; Robinson et al., 2017). However, compound effects of mainshocks and aftershocks are used rarely in the literature (Tanyaş et al., 2022) because estimates of ground shaking generally are only generated for individual events. Here we used the USGS composite PGA map representing the maximum PGA at each location for the mainshocks and aftershocks (>M5.5) as described earlier (Goldberg et al., 2023; Wald et al., 2023).

In general, the intensity of ground shaking tends to decrease with distance from the fault rupture plane. As a result, for strike-slip faults that tend to have a near-vertical dips, landslide concentration tends to decrease nearly symmetrically perpendicular to faults if other susceptibility factors are similar (e.g., Gorum and Carranza, 2015; Keefer, 2000; Fan et al., 2019). Thus, distance to fault is strongly correlated with ground shaking estimates and both are widely used as variables controlling the spatial distribution of coseismic landslides (e.g., Fan et al., 2019; Massey et al., 2018). However, depending on rupture dynamics and fault zone structure, near-field ground motion may also play a factor in landslide generation, so the two are not necessarily redundant (Oral

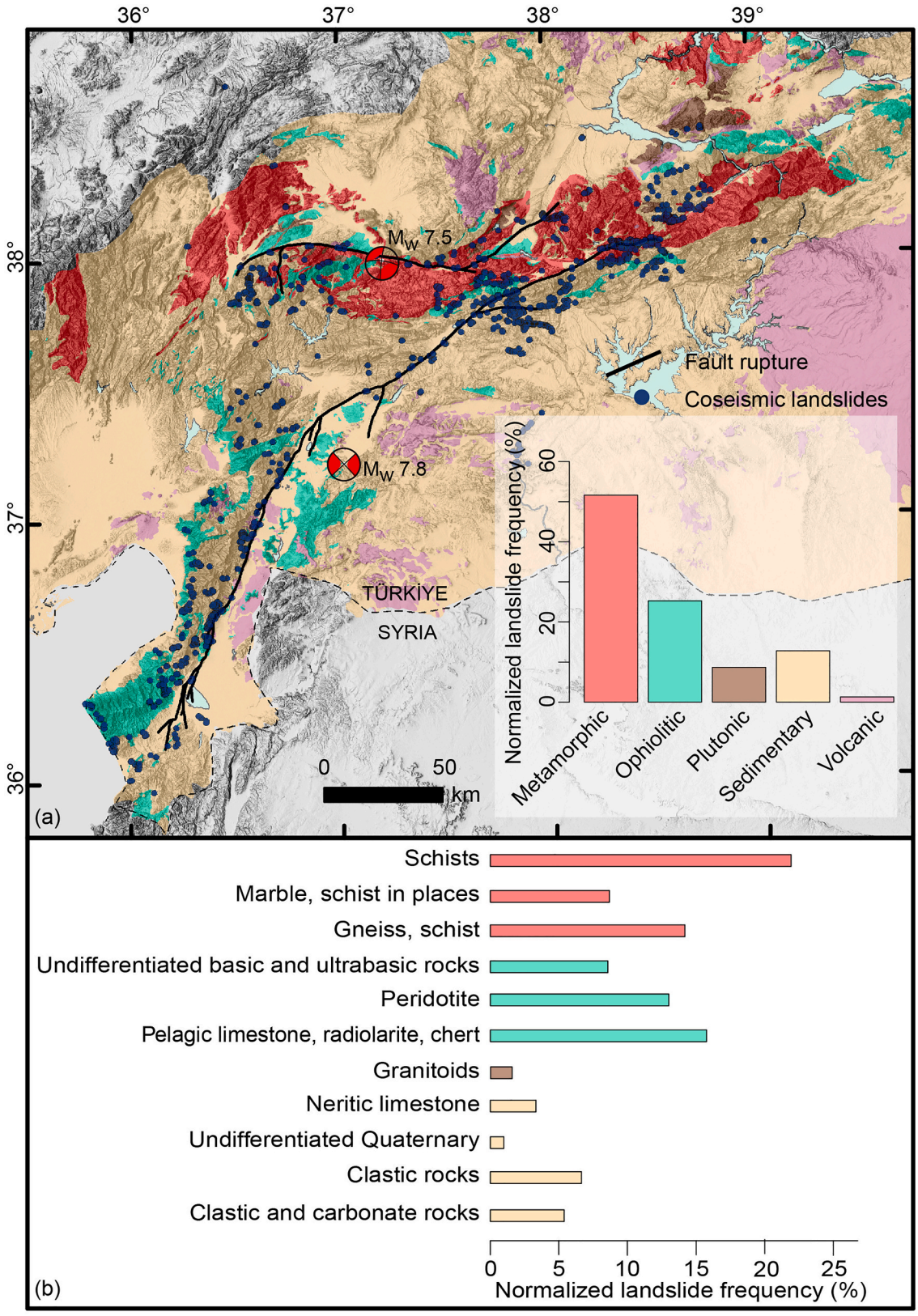

Fig. 9. Spatial and frequency distribution of landslides over (a) aggregated and (b) specific rock types seen in the study area. Landslide frequencies were normalized for the percentage of the study area covered by each of these rock types.

Fig. 10. Drone images showing an area affected by rock falls (lat: 36.67°, lon: 36.43°) near Kırıkhan, Hatay. The red point in panel (a) shows the landslide location. Panels (b) and (c) show the entire hillslopes exposed to rock falls and a house destroyed by a rock fall, respectively. The width of the hillslope was indicated in panel (b) as a bar scale. The viewing angle of panel (c) was indicated in panel (b). (For interpretation of the references to colour in this figure legend, the reader is referred to the web version of this article.)

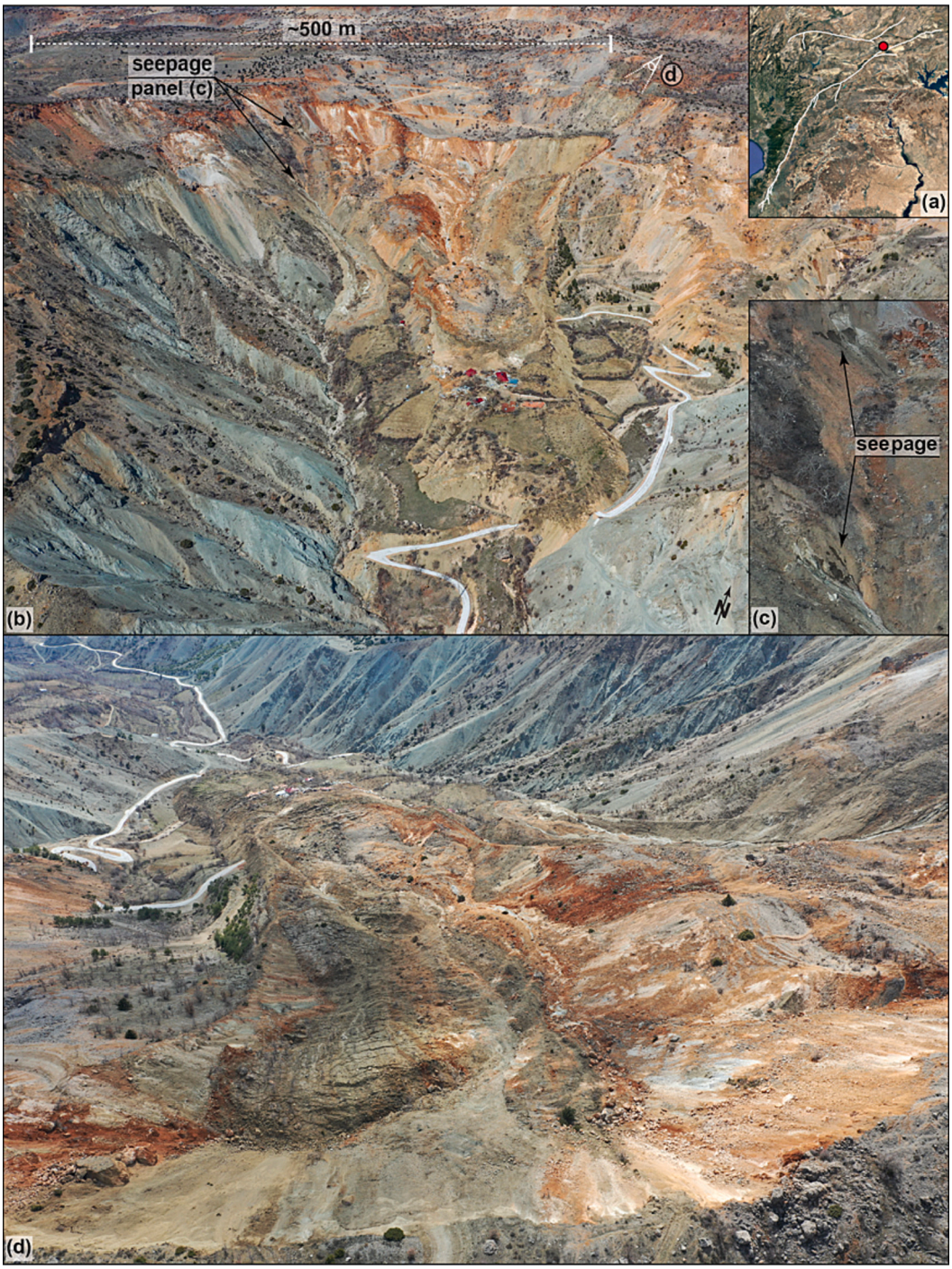

Fig. 11. Drone images showing an example of a bedrock rotational slide (lat: 37.91°, lon: 37.78°) near Dogansehir, Malatya. The red point in panel (a) indicates the landslide location. Panel (c) shows zoom-in view of seepage seen around the boundary of the landslide. Panels (b) and (d) show landslide in upslope and downslope angles, respectively. Panel (c) shows zoom-in view of seepage seen around the boundary of the landslide. The viewing angle of panel (d) was indicated in panel (c). (For interpretation of the references to colour in this figure legend, the reader is referred to the web version of this article.)

et al., 2020).

We run a kernel density estimator (Sheather and Jones, 1991) to assess the distribution of failed locations and the entire landscape for distance to the fault and PGA. Specifically, we used the density function in R (R Core Team, 2020) proving 2-dimensional density estimates based on a Gaussian kernel. We present the characteristics of the terrain with and without flat areas. To identify flat areas, we applied a landform classification algorithm provided by the GRASS GIS module r.geomorphon (Jasiewicz and Stepinski, 2013). The algorithm uses pattern recognition and mainly uses inner (5 grids), outer search (25 grids) radius and flatness (5°) threshold (e.g., Tanyaş and Lombardo, 2019). We also gave examples of some of the mapped coseismic landslides in terms of their consequences such as fatalities or damaged engineering structures.

4. Results

4.1. General characteristics of coseismic landslides

We mapped 3673 coseismic landslides. Our field observations

Fig. 12. Aerial photos showing the translational slide (lat: 36.16°, lon: 36.22°) triggered near Altınözü, Hatay. The red point in panel (a) shows the landslide location. Panels (c) and (d) show the entire landslide body and the crown of the landslide, respectively. The viewing angle of panel (c) was indicated in panel (b). (For interpretation of the references to colour in this figure legend, the reader is referred to the web version of this article.)

suggest that the actual total coseismic landslide population could be significantly greater because smaller landslides were not visible in the imagery and we didnot visit all areas in the field. Also, the snow cover and arid landscape create low-contrast between pre- and post-slide conditions in optical imagery, so identifying additional landslides would require more detailed mapping coupled with field work.

Our findings show that the 0.12-g PGA contour includes >99% of all mapped coseismic landslides, with only 54 located outside of this area (see Fig. 1). The majority of coseismic landslides were triggered close to the rupture zone. >70% of the landslides occurred within a 10-km-wide zone around the faults. A 20-km-wide zone encompasses >90% of landslides (Fig. 6). Therefore, the majority of the landslides were concentrated in a fairly narrow zone along the fault trace where PGA was high.

We further examined the density distribution of landslides with respect to PGA, elevation, slope, and local relief on failed hillslopes compared to the entire landscape (Fig. 7). Landscape characteristics are shown both with and without flat areas. About 70% of the mapped coseismic landslides occurred in areas where PGA ranges from 0.3 to 0.6 g; the peak landslide concentration is in areas where PGA is about 0.6 g. Most landslides (>70%) occurred on hillslopes in an elevation range of 800–1400 m, with slopes of 20–45°, and local relief of 400–700 m.

Additionally, we compared the mapped landslide locations to the USGS GF product estimates of areal coverage (Fig. 2a). We cannot quantitatively compare the two because the GF product estimates the proportion of the ~250 m resolution grid cell expected to be affected by a landslide, and we cannot compute the actual areas of landslide coverage using a point inventory. However, we can compare the landslides to the model qualitatively. A visual comparison suggests the mapped landslides seem to be concentrated around the rupture zone where estimated GF areal coverage values are also elevated. However, the frequency distribution of the landslides show that many landslides

Fig. 13. Drone image showing an area affected by lateral spreading (lat: 37.79°, lon: 37.65°) near Golbasi, Adıyaman. The red point in panel (a) shows the landslide location. Panel (b) shows the area from the top with a bar scale. (For interpretation of the references to colour in this figure legend, the reader is referred to the web version of this article.)

occurred in areas where GF areal coverage values were relatively low (Fig. 2a inset). In particular, many landslides occurred in the far northeast in areas of low GF areal coverage estimates (<1%), which suggests that the shaking is potentially underestimated in this region.

We also analyzed the slope-aspect distribution of failed hillslopes and the entire landscape. Results showed slopes of all azimuths with the greatest concentration in the NNW and SSE direction. Failed slopes faced primarily south (Fig. 8). This could be associated with differences in vegetation type and density that can result in higher causing a relatively high landslide susceptibility on south facing hillslopes in some semi-arid environments in the Northern Hemisphere (e.g., Li et al., 2021; Deng et al., 2022).

Approximately 60% of the landslides occurred in sedimentary rock, 30% in metamorphic rock, and 10% in volcanic rock. However, sedimentary rocks cover >70% of the study area (i.e., area bounded by PGA of 0.12 g). Therefore, we normalized these values for the percentage of the study area covered by each of these rock types. After normalizing, the majority of landslides appeared to be associated with metamorphic rock (51%) and ophiolitic (25%) rocks (Fig. 9). Specifically, schist, gneiss and pelagic limestone are the most susceptible units.

Our field investigations showed that lithologic units and their contact relationships played a role in the spatial distribution of coseismic landslides. We elaborate on this observation with site-specific examples in the following section.

4.2. Types of ground failure

In this section, we use specific examples to describe the most prominent ground-failure phenomena we observed: (1) rock falls, (2) bedrock rotational landslides, (3) translational slides and (iv) lateral spreads.

4.2.1. Rock falls

Rock falls are the most abundant coseismic landslides in the study area. Most originated in limestone, and individual blocks were as large as six to seven meters in some areas. Some of these rock falls hit populated areas and caused financial losses and fatalities. Fig. 10 shows farmland and a house that were damaged extensively by rock falls. Some rock falls traveled as far as 600 m from their source areas.

Rock-fall fatalities were reported in the news and social media. For example, a fatal rock fall in the Bektaşlı village, approximately 5 km south of the Deliçay Demre Lake, was reported to have killed 49 people. However, local residents from the Bektaşlı village informed us that the majority of the deaths were caused by ground shaking and rotational landslides, although some houses were hit by rock falls as well.

4.2.2. Bedrock rotational slides

Bedrock rotational slides also are common in the study area, especially in the north. They were mainly triggered within pre-existing landslides. Our preliminary investigations suggest that failures of deep-seated landslides might have occurred along geologic contacts separating units having different permeabilities. We observed seepage around the crown of some deep landslides (e.g., Fig. 11c), which we interpret to indicate the contact between more permeable geologic units above and less permeable units below. This permeability contrast could cause an increase in pore-water pressure along the contact, which would

Fig. 14. Drone images showing a coseismic landslide occurred along the surface rupture (lat: 38.06°, lon: 36.99°) near Ekinözü, Kahramanmaraş. The red point in panel (a) shows the landslide location. Panels (b-c) and (d) show surface rupture and zoom-in view of landslide location, respectively. The viewing angles of panels (c) and (d) were indicated in panel (b). (For interpretation of the references to colour in this figure legend, the reader is referred to the web version of this article.)

Fig. 15. An incipient landslide (lat: 38.03°, lon: 37.18°) near Ekinözü, Kahramanmaraş. The red point in panel (a) shows the location of the selected hillslope. Panels (b) and (c) show the landslide location from different angles. The viewing angle of panel (c) was indicated in panel (b) (For interpretation of the references to colour in this figure legend, the reader is referred to the web version of this article.)

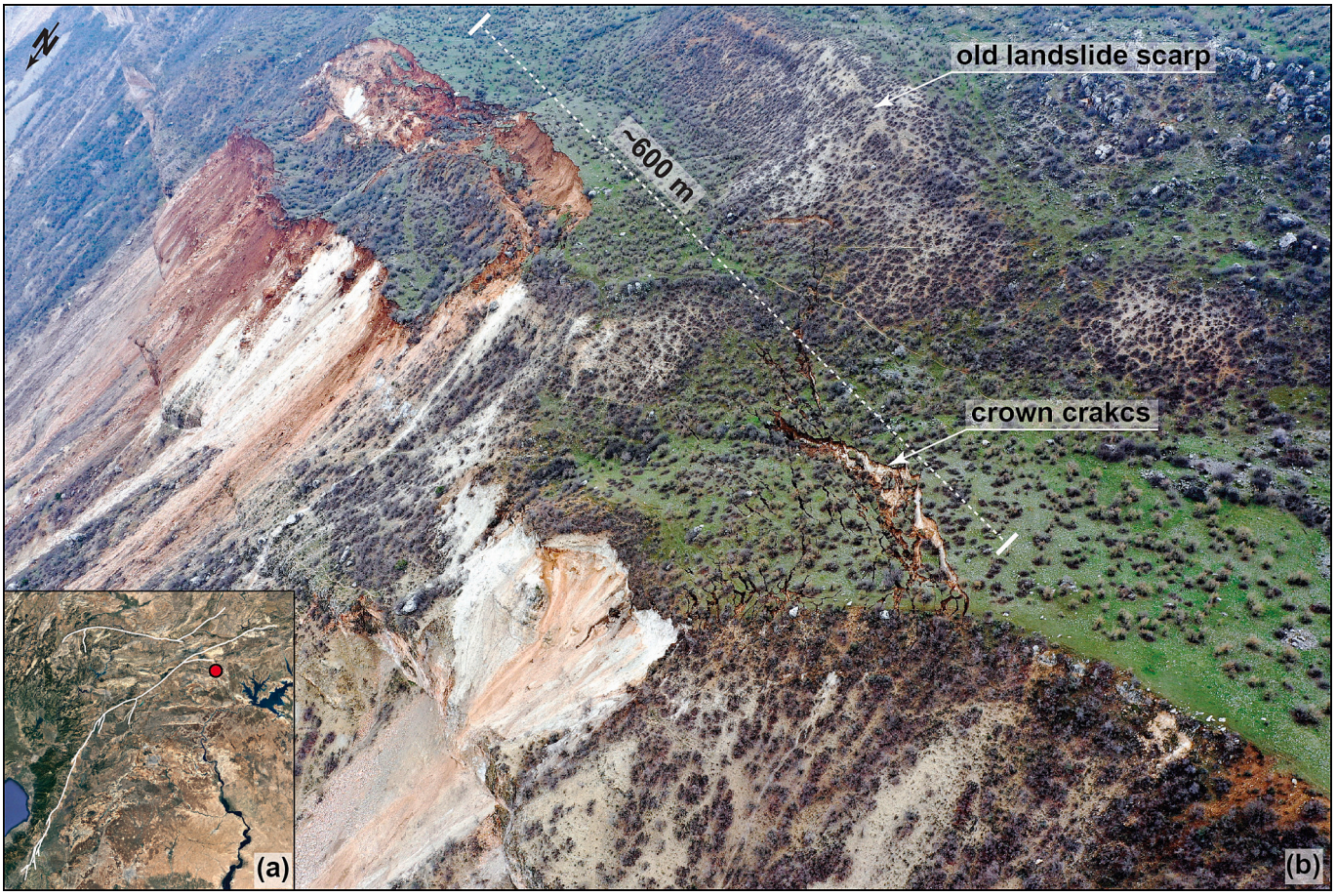

Fig. 16. The drone image showing an example of a crown crack (lat: 37.75°, lon: 37.98°) near Tut, Adıyaman. The red point in panel (a) shows the location of the selected hillslope. Panel (b) shows the landslide location from the top with a bar scale. (For interpretation of the references to colour in this figure legend, the reader is referred to the web version of this article.)

decrease the frictional resistance to sliding and contribute to slope failure.

The Incirlik landslide, with an area of ~1.2 km^2, is one of the largest mapped so far. This landslide occurred in the north, in Dogansehir, Malatya. Incirlik is the name of the village where dozens of houses were built on the slope of an ancient landslide (Fig. 11b). Metamorphic rock, primarily marble, outcrops near the crown of the ancient landslide. In the lower sectors of this slide, permeable sedimentary rock is in contact with ophiolite. The failure seems to have been triggered along this contact. Based on local accounts, we know the landslide occurred during the main earthquake shock in the early morning of February 6. No one died in this landslide, but the entire village moved approximately 450 m downslope. Most houses were damaged or buried, but the residents had time to move outside during the failure. This indicates that the failure occurred relatively slowly. The landslide blocked both a road and a river channel but did not impound any water.

4.2.3. Translational slides

An example of translational landslide is in Tepehan village near Altınözü, Hatay. A landslide with an area of ~1.3 km2 occurred in marl and clay-rich limestone. The slide formed deep cracks along undulating hillslopes (Fig. 12). The thickness of the failure is 20 m, and the sliding basal surface is the upper bedding surface of a clay-rich limestone unit interbedded with marl, which is intensely weathered in the upper parts (Sümer et al., 2023).

4.2.4. Lateral spreading

Lateral spreading was the most common in the south, in Hatay province. This is because slopes in this area are gentler, and the soils are more loose and sandy (Taftsoglou et al., 2023). Lateral spreading also occurred in some flat areas in the central sector but was not observed in the north where the slopes are steeper (Taftsoglou et al., 2023). One of the most notable examples of lateral spreading in the central area occurred at Golbasi Lake, located in Adıyaman. In this case, the lateral spreading caused several buildings to collapse and sink into the lake (Fig. 13).

4.3. Landslides associated with surface rupture

As indicated above, the earthquake sequence caused a long surface rupture, cumulatively >500 km. In some areas where surface rupture crossed through mountainous terrain, numerous landslides crowned along the surface rupture. Some of these landslides caused fatalities.

The 0.5km^2 Tepebasi landslide is an example of the destructive power of landslides triggered by this mechanism. The earth slide killed eight people and buried or damaged several houses (Fig. 14). It occurred in highly weathered volcanic rock. Drone images in Fig. 14 show how surface rupture extends just above the Tepebasi village and forms the upper part of the sliding surface.

4.4. Incipient landslides and crown cracks

Strong shaking disturbed the ground surface in many areas, particularly in the north, and created pervasive extensional cracks. For instance, incipient landslides are particularly common in the north along the rupture zone of the second earthquake. They were mainly

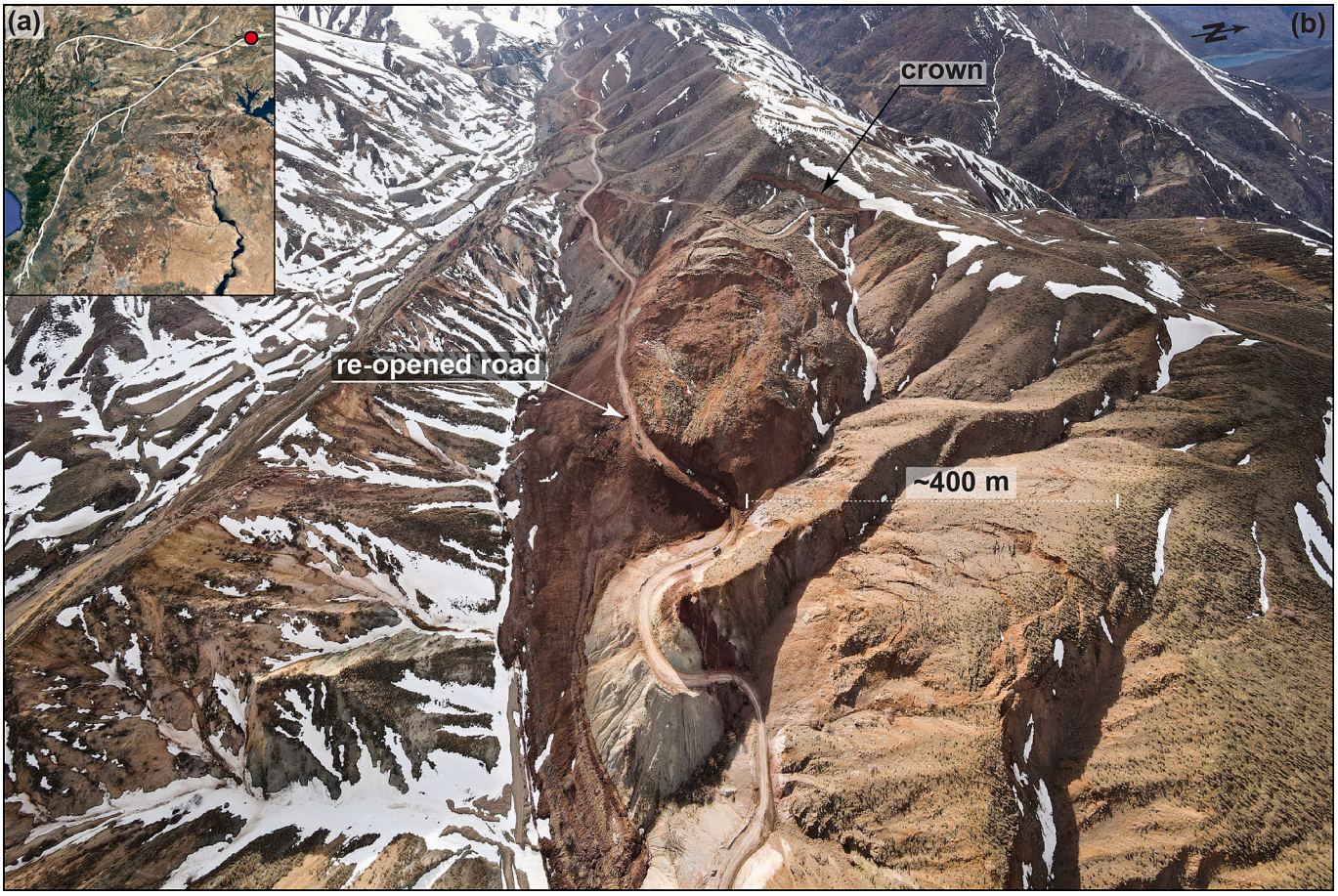

Fig. 17. View of the main road connecting the mountainous hamlets and district blocked by coseismic landslides (lat: 38.05°, lon: 38.36°) near Adıyaman. The red point in panel (a) shows the landslide location. Panel (b) shows the road, failed landslide and crown cracks. (For interpretation of the references to colour in this figure legend, the reader is referred to the web version of this article.)

formed in massive limestone units along ridges crests adjacent to the fault rupture. Fig. 15 shows the crown of an incipient landslide crossing the entire hillslope along ridges crests around the Ekinözü, Kahramanmaraş region close to the epicenter of the second earthquake. The vertical displacements along the crown reach up to a few meters, and some surface deformations were also visible toward the lower part of the same hillslope.

We documented some crown cracks and the Çekirge Dağı region provides a good example (Fig. 16). These hillslopes are located in the central part of the area close to Tut, Adıyaman. The 2023 earthquake opened new tension cracks within neritic limestone forming the steep upper part of these hillslopes. The lower parts of the hillslope consist of weak clastic rocks, resulting in smoother topography. A pre-existing landslide crown, on the other hand, is visible at the upper part of the hillslope.

Notably, these highly deformed hillslopes will be more prone to landslides in the post-seismic period, and in this regard, they are the direct manifestation of the earthquake legacy effect in the area (Kincey et al., 2021; Parker et al., 2015; Tanyaş et al., 2021).

4.5. Major consequences of landslides

Coseismic ground failure caused fatalities, large financial losses, and infrastructure damage. In this section, we present a few cases that demonstrate the range of the resulting societal consequences.

4.5.1. Blocked roads

Blocked roads are a common consequence of coseismic landslides (e.g., Harp and Jibson, 1996; Kargel et al., 2016; Kieffer et al., 2006) hampering not only emergency response actions following the earthquake but also recovery in the post-seismic phase. A striking example that occurred in Çelikhan, Adıyaman, toward the northeastern edge of the first earthquake fault rupture, shows how problematic blocked roads can be. Many landslides were triggered in this area by the mainshock, some of them fatal. For instance, in Mutlu village (Çelikhan, Adiyaman) 49 people were killed by the compound effect of collapsed buildings and coseismic landslides. In this mountainous terrain, only two roads access Mutlu village, and both of those roads were blocked by landslides at several locations. Fig. 17 shows one of those road sectors blocked by a large coseismic landslide in highly weathered metamorphic rock. A ~ 500 m long section of the road was blocked on February 6 and remained closed until early March. Reopening the road took more than a month because the landslide body was still prone to reactivation, and thus removal of the toe material was difficult and risky. This hampered post-seismic disaster response operations.

4.5.2. Blocked river channels

The blockage of river channels by coseismic landslides that form natural dams is also a common phenomenon after strong earthquakes (Fan et al., 2012; Parvaiz et al., 2012). In the post-seismic period, the failure of those dams could cause cascading hazards (Fan et al., 2019). Although few landslide dams formed following the February 6 earthquake sequence, they still require attention as their failure could cause flooding downstream.

A landslide dam formed in the south of the earthquake-affected area, close to Islahiye. The landslide was triggered in limestone by the

Fig. 18. Aerial photos showing an example of a landslide dam (lat: 37.00°, lon: 36.59°) near Islahıye, Gaziantep. The red point in panel (a) shows the landslide location. Panel (b) and (c) show landslide body from different angles. The viewing angle of panel (c) was indicated in panel (b). (For interpretation of the references to colour in this figure legend, the reader is referred to the web version of this article.)

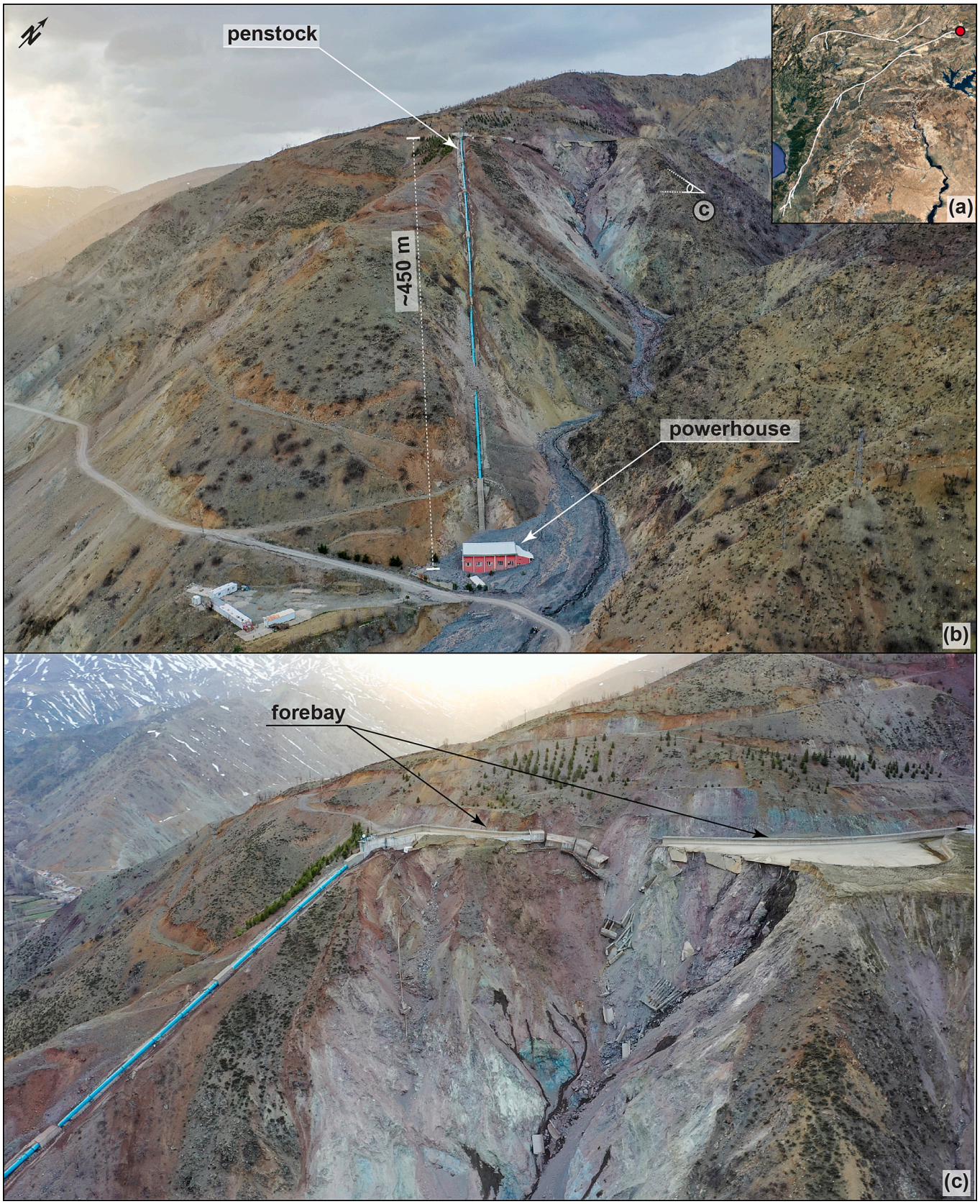

Fig. 19. Aerial photos showing a hydroelectric power plant hit by a coseismic landslide (lat: 38.05°, lon: 38.42°) near Çelikhan, Adıyaman. The red point in panel (a) shows the landslide location. Panel (b) shows both penstock and powerhouse, while panel (b) presents the destroyed forebay. The viewing angle of panel (c) was indicated in panel (b). (For interpretation of the references to colour in this figure legend, the reader is referred to the web version of this article.)

mainshock, and water impounded rapidly behind the dam in the following month (Fig. 18). The General Directorate of State Hydraulic Works (DSI) opened a spillway on top of the landslide dam to reduce the lake level and prevent failure of the dam. However, a settlement downstream appears to be at risk from flooding if failure were to occur.

The rock slide that formed the dam is one of the largest (~1.2 km2) landslides in the south. Most landslides near the landslide dam are much smaller rock falls and shallow landslides. An open pit mine has been operating directly upslope of the failed hillslope for approximately the last 10 years, which might have influenced the stability of the slope that failed due to blasting operations.

4.5.3. *Destroyed engineering structures*

Coseismic landslides also caused financial losses from damaged infrastructure (e.g., hydroelectric power plants) and farmland. The power plant located in Askerhan village (Çelikhan, Adıyaman), toward the north end of the first earthquake fault rupture, was destroyed by a landslide in ophiolite (Fig. 19). The slide collapsed the forebay structure, and continued runout then hit the powerhouse, which was partially buried under the debris. Some minor failures also occurred along the penstock. Therefore, due to landsliding, the plant was destroyed and is no longer operational.

5. Conclusions

This study presented our preliminary observations regarding the landslides triggered by the 2023 Türkiye earthquake sequence. We analyzed satellite and aerial imagery covering the earthquake-affected area and supplemented our remote observations with field investigations. We mapped 3673 coseismic landslides associated with this event, making this the largest, documented coseismic landslide event in Türkiye.

>90% of the mapped landslides occurred in a 20-km-wide zone along the fault rupture. Rock falls, bedrock rotational landslides, and lateral spreads are the main landslide types present. Among these types, rock falls were triggered over the entire area, whereas bedrock rotational landslides are mainly present in the north, lateral spreads in the south. Incipient landslides and highly deformed hillslopes were also widely observed in the earthquake-affected area.

Given the abundance of coseismic landslides and incipient landslides, an increase in landslide frequency in the post-seismic period is likely. This has been observed in many other landscapes affected by strong earthquakes (Chen et al., 2020; Fan et al., 2018; Tian et al., 2020). Therefore, parts of the earthquake-affected area that are most prone to such ongoing hazard could be monitored using both remote sensing and in-situ measurements.

This event could also provide a valuable contribution to our overall understanding of coseismic landslides in semi-arid areas. The global earthquake-induced ground failure repository (Schmitt et al., 2017; Tanyaş et al., 2017) includes only a few examples (e.g., the 1994 Northridge and 2010 Sierra Cucapah earthquakes) characterizing coseismic landslide events that occurred in arid/semi-arid conditions. Therefore, models developed based on those inventories, such as the one used by the USGS GF Product (Nowicki Jessee et al., 2018), are missing potentially important climatic factors associated with physical weathering caused by different climatic conditions. In this context, identifying the spatial distribution of landslides in this earthquake sequence could help us to upgrade our predictive capacity for future earthquake-induced landslides in areas having arid/semi-arid conditions.

Funding

This work was funded by the NATO Science for Peace and Security Program (SPS project G6190), Foundation for the Development of ITU, University of Twente, the Department of Applied Earth Science of ITC, the U.S. Geological Survey and the U.S. Agency for International Development (USAID) Bureau of Humanitarian Assistance.

CRediT authorship contribution statement

Tolga Görüm: Writing – review & editing, Writing – original draft, Visualization, Investigation, Funding acquisition, Formal analysis, Data curation, Conceptualization. **Hakan Tanyas:** Visualization, Data curation, Conceptualization, Formal analysis, Funding acquisition, Investigation, Writing – original draft, Writing – review & editing. **Furkan Karabacak:** Visualization, Resources. **Abdüssamet Yılmaz:** Visualization, Formal analysis. **Serkan Girgin:** Software, Investigation, Formal analysis. **Kate E. Allstadt:** Visualization, Conceptualization, Investigation, Writing – review & editing. **M. Lütfi Süzen:** Investigation. **Paula Burgi:** Writing – review & editing, Investigation.

Declaration of Competing Interest

The authors declare that they have no known competing financial interests or personal relationships that could have appeared to influence the work reported in this paper.

Data availability

The landslide inventory will be shared through Supplementary Materials upon the acceptance of the manuscript.

Acknowledgments

We would like to express our deepest condolences to the victims of the earthquake sequence. We are grateful to all the local people who provided information regarding the details of this disastrous event. We are grateful for constructive reviews by Randall W. Jibson and three anonymous reviewers. We thank the Istanbul Technical University, Implementation and Research Center for Satellite Communications and Remote Sensing (CSCRS) for supporting SPOT satellite data, especially Prof. Dr. Nebiye Musaoglu for her kind support. MAXAR images were acquired from MAXAR's open Data Program, https://www.maxar.com/open-data/turkey-earthquake-2023.Any use of trade, firm, or product names is for descriptive purposes only and does not imply endorsement by the U.S. Government.

Appendix A. Supplementary data

Supplementary data to this article can be found online at https://doi.org/10.1016/j.enggeo.2023.107315.

References

Abdelmeguid, M., Zhao, C., Yalcinkaya, E., Gazetas, G., Elbanna, A., Rosakis, A., 2023. Revealing the Dynamics of the Feb 6th 2023 M7. 8 Kahramanmara/Pazarcik Earthquake: near-field records and dynamic rupture modeling. arXiv Prepr. arXiv2305.01825. https://doi.org/10.48550/arXiv.2305.01825.

Aktug, B., Ozener, H., Dogru, A., Sabuncu, A., Turgut, B., Halicioglu, K., Yilmaz, O., Havazli, E., 2016. Slip rates and seismic potential on the East Anatolian Fault System using an improved GPS velocity field. J. Geodyn. 94–95, 1–12. https://doi.org/10.1016/j.jog.2016.01.001.

Allstadt, K.E., Thompson, E.M., Jibson, R.W., Wald, D.J., Hearne, M., Hunter, E.J., Fee, J., Schovanec, H., Slosky, D., Haynie, K.L., 2022. The US Geological Survey ground failure product: near-real-time estimates of earthquake-triggered landslides and liquefaction. Earthquake Spectra 38, 5–36.

Ambraseys, N.N., 1989. Temporary seismic quiescence: SE Turkey. Geophys. J. Int. 96, 311–331. https://doi.org/10.1111/j.1365-246X.1989.tb04453.x.

Ambraseys, N., 2009. Earthquakes in the Mediterranean and Middle East: A Multidisciplinary Study of Seismicity up to 1900. Cambridge University Press.

Arpat, E., 1971. Arpat, A. E. 1971. 22 Mayıs, 1971 Bingöl Depremi Ön Raporu. Inst. Miner. Res. Explor. Rep. 4697.

Arpat, E., Şaroğlu, F., 1972. Doğu Anadolu Fayı ile ilgili bazı gözlem ve düşünceler. MTA Derg. 78, 44–50.

Arpat, E., Şaroğlu, F., 1975. Türkiye'deki bazı önemli genç tektonik olaylar. Türkiye Jeol. Kurumu Bülteni 18, 91–101.

Bozkurt, E., Mittwede, S.K., 2001. Introduction to the geology of Turkey—a synthesis. Int. Geol. Rev. 43, 578–594. https://doi.org/10.1080/00206810109465034.
Chen, M., Tang, C., Xiong, J., Shi, Q.Y., Li, N., Gong, L.F., Wang, X.D., Tie, Y., 2020. The long-term evolution of landslide activity near the epicentral area of the 2008 Wenchuan earthquake in China. Geomorphology 367, 107317. https://doi.org/10.1016/j.geomorph.2020.107317.
Deng, J., Ma, C., Zhang, Y., 2022. Shallow landslide characteristics and its response to vegetation by example of July 2013, extreme rainstorm, Central Loess Plateau, China. Bull. Eng. Geol. Environ. 81 (3), 100. https://doi.org/10.1007/s10064-022-02606-1.
Dewey, J.F., Hempton, M.R., Kidd, W.S.F., Saroglu, F., Şengör, A.M.C., 1986. Shortening of continental lithosphere: the neotectonics of Eastern Anatolia—a young collision zone. Geol. Soc. Lond. Spec. Publ. 19, 1–36.
Duman, T.Y., Emre, Ö., 2013. The East Anatolian Fault: geometry, segmentation and jog characteristics. Geol. Soc. Lond. Spec. Publ. 372, 495–529.
Emre, Ö., Duman, T.Y., Özalp, S., Elmacı, H., Olgun, Ş., Şaroğlu, F., 2013. Açıklamalı Türkiye Diri Fay Haritası. Ölçek 1.
Fan, X., van Westen, C.J., Xu, Q., Gorum, T., Dai, F., 2012. Analysis of landslide dams induced by the 2008 Wenchuan earthquake. J. Asian Earth Sci. 57, 25–37. https://doi.org/10.1016/j.jseaes.2012.06.002.
Fan, X., Domènech, G., Scaringi, G., Huang, R., Xu, Q., Hales, T.C., Dai, L., Yang, Q., Francis, O., 2018. Spatio-temporal evolution of mass wasting after the 2008 Mw 7.9 Wenchuan earthquake revealed by a detailed multi-temporal inventory. Landslides 15, 2325–2341. https://doi.org/10.1007/s10346-018-1054-5.
Fan, X., Scaringi, G., Korup, O., West, A.J., van Westen, C.J., Tanyas, H., Hovius, N., Hales, T.C., Jibson, R.W., Allstadt, K.E., Zhang, L., Evans, S.G., Xu, C., Li, G., Pei, X., Xu, Q., Huang, R., 2019. Earthquake-induced chains of Geologic Hazards: patterns, mechanisms, and impacts. Rev. Geophys. 57, 421–503. https://doi.org/10.1029/2018RG000626.
Gallen, S.F., Clark, M.K., Godt, J.W., Roback, K., Niemi, N.A., 2017. Application and evaluation of a rapid response earthquake-triggered landslide model to the 25 April 2015 Mw 7.8 Gorkha earthquake, Nepal. Tectonophysics 714–715, 173–187. https://doi.org/10.1016/j.tecto.2016.10.031.
GMAO (Global Modeling and Assimilation Office), 2015. MERRA-2 tavgM_2d_slv_Nx: 2d, Monthly mean,Time-Averaged,Single-Level,Assimilation,Single-Level Diagnostics V5.12.4, Greenbelt, MD, USA, Goddard Earth Sciences Data and Information Services Center (GES DISC) [WWW Document]. https://doi.org/10.5067/AP1B0BA5PD2K.
Goldberg, D.E., Taymaz, T., Reitman, N.G., Hatem, A.E., Yolsal-Çevikbilen, S., Barnhart, W.D., Irmak, T.S., Wald, D.J., Öcalan, T., Yeck, W.L., Özkan, B., Thompson Jobe, J.A., Shelly, D.R., Thompson, E.M., DuRoss, C.B., Earle, P.S., Briggs, R.W., Benz, H., Erman, C., Doğan, A.H., Altuntaş, C., 2023. Rapid Characterization of the February 2023 Kahramanmaraş, Türkiye, Earthquake Sequence. Seism. Rec. 3, 156–167. https://doi.org/10.1785/0320230009.
Görüm, T., 2016. 23 Ekim 2011 Van Depreminin Tetiklediği Heyelanlar. Türk CoğrafyaDergisi 0. https://doi.org/10.17211/tcd.69854.
Gorum, T., Carranza, E.J.M., 2015. Control of style-of-faulting on spatial pattern of earthquake-triggered landslides. Int. J. Environ. Sci. Technol. 12, 3189–3212. https://doi.org/10.1007/s13762-015-0752-y.
Gorum, T., van Westen, C.J., Korup, O., van der Meijde, M., Fan, X., van der Meer, F.D., 2013. Complex rupture mechanism and topography control symmetry of mass-wasting pattern, 2010 Haiti earthquake. Geomorphology 184, 127–138. https://doi.org/10.1016/j.geomorph.2012.11.027.
Harp, E.L., Jibson, R.W., 1996. Landslides triggered by the 1994 Northridge, California, earthquake. Bull. Seismol. Soc. Am. 86, S319–S332.
Herece, E., 2008. Doğu Anadolu Fayı (DAF) Atlası., in: General Directorate of Mineral Research and Exploration. Special Publications, Ankara, Serial Number, 13, p. 359.
Jasiewicz, J., Stepinski, T.F., 2013. Geomorphons — a pattern recognition approach to classification and mapping of landforms. Geomorphology 182, 147–156. https://doi.org/10.1016/j.geomorph.2012.11.005.
Jibson, R.W., Harp, E.L., 2016. Ground motions at the outermost limits of seismically triggered landslides. Bull. Seismol. Soc. Am. 106, 708–719. https://doi.org/10.1785/0120150141.
Jibson, R.W., Harp, E.L., Michael, J.A., 2000. A method for producing digital probabilistic seismic landslide hazard maps. Eng. Geol. 58, 271–289. https://doi.org/10.1016/S0013-7952(00)00039-9.
Karabacak, V., Özkaymak, Ç., Sözbilir, H., Tatar, O., Aktuğ, B., Özdağ, Ö.C., Çakir, R., Aksoy, E., Koçbulut, F., Softa, M., 2023. The 2023 Pazarcık (Kahramanmaraş, Türkiye) earthquake (Mw 7.7): implications for surface rupture dynamics along the East Anatolian Fault Zone. J. Geol. Soc. 180, jgs2023–020. https://doi.org/10.1144/jgs2023-020.
Karakas, G., Nefeslioglu, H.A., Kocaman, S., Buyukdemircioglu, M., Yurur, T., Gokceoglu, C., 2021. Derivation of earthquake-induced landslide distribution using aerial photogrammetry: the January 24, 2020, Elazig (Turkey) earthquake. Landslides 18, 2193–2209. https://doi.org/10.1007/s10346-021-01660-2.
Kargel, J.S., Leonard, G.J., Shugar, D.H., Haritashya, U.K., Bevington, A., Fielding, E.J., Fujita, K., Geertsema, M., Miles, E.S., Steiner, J., Anderson, E., Bajracharya, S., Bawden, G.W., Breashears, D.F., Byers, A., Collins, B., Dhital, M.R., Donnellan, A., Evans, T.L., Geai, M.L., Glasscoe, M.T., Green, D., Gurung, D.R., Heijenk, R., Hilborn, A., Hudnut, K., Huyck, C., Immerzeel, W.W., Jiang, L., Jibson, R., Kääb, A., Khanal, N.R., Kirschbaum, D., Kraaijenbrink, P.D.A., Lamsal, D., Liu, S., Lv, M., McKinney, D., Nahirnick, N.K., Nan, Z., Ojha, S., Olsenholler, J., Painter, T.H., Pleasants, M., Pratima, K.C., Yuan, Q.I., Raup, B.H., Regmi, D., Rounce, D.R., Sakai, A., Shangguan, D., Shea, J.M., Shrestha, A.B., Shukla, A., Stumm, D., Van Der Kooij, M., Voss, K., Wang, X., Weihs, B., Wolfe, D., Wu, L., Yao, X., Yoder, M.R., Young, N., 2016. Geomorphic and geologic controls of geohazards induced by Nepal's 2015 Gorkha earthquake. Science (80) 351. https://doi.org/10.1126/science.aac8353.
Kaymakci, N., Inceöz, M., Ertepinar, P., Koç, A., 2010. Late cretaceous to recent kinematics of SE Anatolia (Turkey). Geol. Soc. Lond. Spec. Publ. 340, 409–435.
Keefer, D.K., 2000. Statiscal analysis of an earthquake-induced landslide distribution - the 1989 Loma Prieta, California event. Eng. Geol. 58, 231–249. https://doi.org/10.1016/S0013-7952(00)00037-5.
Kieffer, D.S., Jibson, R., Rathje, E.M., Kelson, K., 2006. Landslides Triggered by the 2004 Niigata Ken Chuetsu, Japan. Earthquake. Earthq. Spectra 22, 47–73. https://doi.org/10.1193/1.2173021.
Kincey, M.E., Rosser, N.J., Robinson, T.R., Densmore, A.L., Shrestha, R., Pujara, D.S., Oven, K.J., Williams, J.G., Swirad, Z.M., 2021. Evolution of coseismic and post-seismic landsliding after the 2015 Mw 7.8 Gorkha earthquake, Nepal. J. Geophys. Res. Earth Surf. https://doi.org/10.1029/2020JF005803 e2020JF005803.
Köküm, M., İnceöz, M., 2018. Structural analysis of the northern part of the East Anatolian Fault System. J. Struct. Geol. 114, 55–63. https://doi.org/10.1016/j.jsg.2018.06.016.
Kurcer, A., Elmacı, H., Özdemir, E., Güven, C., Güler, T., Avcu, İ., Olgun, Ş., Avcı, H., Aydoğan, H., Yüce, A., Çetin, F.E., Ayrancı, A., Akyol, Z.S.Ö., Altuntaş, G., Demirörs, U., Karayazı, O., Bayrak, A., Özalp, S., 2023. 06 Şubat 2023 Pazarcık (Kahramanmaraş) Depremi (Mw 7,8) Saha Gözlemleri ve Değerlendirmeler. MTA Genel Müdürlüğü, Rapor No: 14138, 187 s., Ankara (In Turkish).
Li, M., Ma, C., Du, C., Yang, W., Lyu, L., Wang, X., 2021. Landslide response to vegetation by example of July 25–26, 2013, extreme rainstorm, Tianshui, Gansu Province, China. Bull. Eng. Geol. Environ. 80 (2), 751–764. https://doi.org/10.1007/s10064-020-02000-9.
Li, S., Wang, X., Tao, T., Zhu, Y., Qu, X., Li, Z., Huang, J., Song, S., 2023. Source Model of the 2023 Turkey Earthquake Sequence Imaged by Sentinel-1 and GPS Measurements: Implications for Heterogeneous Fault Behavior along the East Anatolian Fault Zone. Remote Sens. https://doi.org/10.3390/rs15102618.
Lionello, P., Malanotte-Rizzoli, P., Boscolo, R., Alpert, P., Artale, V., Li, L., Luterbacher, J., May, W., Trigo, R., Tsimplis, M., Ulbrich, U., Xoplaki, E., 2006. The Mediterranean climate: an overview of the main characteristics and issues. In: Lionello, P., Malanotte-Rizzoli, P., Boscolo, R.B.T.-D. in E. and E.S. (Eds.), Mediterranean. Elsevier, pp. 1–26. https://doi.org/10.1016/S1571-9197(06)80003-0.
Mai, P.M., Aspiotis, T., Aquib, T.A., Cano, E.V., Castro-Cruz, D., Espindola-Carmona, A., Li, B., Li, X., Liu, J., Matrau, R., 2023. The destructive Earthquake Doublet of 6 February 2023 in South-Central Türkiye and Northwestern Syria: initial observations and analyses. Seism. Rec. 3, 105–115.
Massey, C., Townsend, D., Rathje, E., Allstadt, K.E., Lukovic, B., Kaneko, Y., Bradley, B., Wartman, J., Jibson, R.W., Petley, D.N., Horspool, N., Hamling, I., Carey, J., Cox, S., Davidson, J., Dellow, S., Godt, J.W., Holden, C., Jones, K., Kaiser, A., Little, M., Lyndsell, B., McColl, S., Morgenstern, R., Rengers, F.K., Rhoades, D., Rosser, B., Strong, D., Singeisen, C., Villeneuve, M., 2018. Landslides triggered by the 14 November 2016 Mw 7.8 Kaikōura earthquake, New Zealand. Bull. Seismol. Soc. Am. 108, 1630–1648. https://doi.org/10.1785/0120170305.
McKenzie, D., 1972. Active Tectonics of the Mediterranean Region. Geophys. J. Int. 30, 109–185. https://doi.org/10.1111/j.1365-246X.1972.tb02351.x.
McKenzie, D., 1976. The East Anatolian Fault: a major structure in Eastern Turkey. Earth Planet. Sci. Lett. 29, 189–193. https://doi.org/10.1016/0012-821X(76)90038-8.
Melgar, D., Taymaz, T., Ganas, A., Crowell, B.W., Öcalan, T., Kahraman, M., Tsironi, V., Yolsal-Çevikbil, S., Valkaniotis, S., Irmak, T.S., 2023. Sub-and super-shear ruptures during the 2023 Mw 7.8 and Mw 7.6 earthquake doublet in SE Türkiye. Seismica 2 (3). https://doi.org/10.26443/seismica.v2i3.387.
MTA, 2002. 1: 500,000 Scaled Turkish Geology Map Series. MTA Genel Mudurlugu, Ankara.
Nowicki Jessee, M.A., Hamburger, M.W., Allstadt, K., Wald, D.J., Robeson, S.M., Tanyas, H., Hearne, M., Thompson, E.M., 2018. A global empirical model for near-real-time assessment of seismically induced landslides. Case Rep. Med. 123, 1835–1859. https://doi.org/10.1029/2017JF004494.
Okuwaki, R., Yuji, Y., Taymaz, T., Hicks, S.P., 2023. Multi-Scale Rupture Growth with Alternating Directions in a Complex Fault Network during the 2023 South-Eastern Türkiye and Syria Earthquake Doublet. Geophysical Research Letters 50, e2023GL103480. https://doi.org/10.1029/2023GL103480.
Oral, E., Weng, H., Ampuero, J.P., 2020. Does a Damaged-Fault Zone Mitigate the Near-Field Impact of Supershear Earthquakes?—Application to the 2018 7.5 Palu, Indonesia, earthquake. Geophys. Res. Lett. 47, e2019GL085649 https://doi.org/10.1029/2019GL085649.
Parker, R.N., Hancox, G.T., Petley, D.N., Massey, C.I., Densmore, A.L., Rosser, N.J., 2015. Spatial distributions of earthquake-induced landslides and hillslope preconditioning in the northwest South Island, New Zealand. Earth Surf. Dyn. 3, 501–525. https://doi.org/10.5194/esurf-3-501-2015.
Parvaiz, I., Champatiray, P.K., Bhat, F.A., Dadhwal, V.K., 2012. Earthquake-induced landslide dam in the Kashmir Himalayas. Int. J. Remote Sens. 33, 655–660.
Peel, M.C., Finlayson, B.L., McMahon, T.A., 2007. Updated world map of the Köppen-Geiger climate classification. Hydrol. Earth Syst. Sci. 11, 1633–1644. https://doi.org/10.5194/hess-11-1633-2007.
R Core Team. R: A Language and Environment for Statistical Computing. R Foundation for Statistical Computing. https://www.R-project.org/.
Reilinger, R., McClusky, S., Vernant, P., Lawrence, S., Ergintav, S., Cakmak, R., Ozener, H., Kadirov, F., Guliev, I., Stepanyan, R., Nadariya, M., Hahubia, G., Mahmoud, S., Sakr, K., ArRajehi, A., Paradissis, D., Al-Aydrus, A., Prilepin, M., Guseva, T., Evren, E., Dmitrotsa, A., Filikov, S.V., Gomez, F., Al-Ghazzi, R., Karam, G., 2006. GPS constraints on continental deformation in the Africa-Arabia-Eurasia continental collision zone and implications for the dynamics of plate

interactions. J. Geophys. Res. Solid Earth 111. https://doi.org/10.1029/2005JB004051.
Reitman, N.G., Briggs, R.W., Barnhart, W.D., Thompson Jobe, J.A., DuRoss, C.B., Hatem, A.E., Gold, R.D., Akçiz, S., Koehler, R.D., Mejstrik, J.D., Collett, C., 2023, Fault rupture mapping of the 6 February 2023 Kahramanmaraş, Türkiye, earthquake sequence from satellite data: U.S. Geological Survey data release, https://doi.org/10.5066/P985I7U2.
Roback, K., Clark, M.K., West, A.J., Zekkos, D., Li, G., Gallen, S.F., Chamlagain, D., Godt, J.W., 2018. The size, distribution, and mobility of landslides caused by the 2015 Mw7.8 Gorkha earthquake, Nepal. Geomorphology 301, 121–138. https://doi.org/10.1016/j.geomorph.2017.01.030.
Robinson, T.R., Rosser, N.J., Densmore, A.L., Williams, J.G., Kincey, M.E., Benjamin, J., Bell, H.J.A., 2017. Rapid post-earthquake modelling of coseismic landslide intensity and distribution for emergency response decision support. Nat. Hazards Earth Syst. Sci. 17, 1521–1540. https://doi.org/10.5194/nhess-17-1521-2017.
Schmitt, R.G., Tanyas, H., Nowicki Jessee, M.A., Zhu, J., Biegel, K.M., Allstadt, K.E., Jibson, R.W., Thompson, E.M., van Westen, C.J., Sato, H.P., Wald, D.J., Godt, J.W., Gorum, T., Xu, C., Rathje, E.M., Knudsen, K.L., 2017. An Open Repository of Earthquake-Triggered Ground-Failure Inventories, Data Series. Reston, VA. https://doi.org/10.3133/ds1064.
Şengör, A.M.C., Yazıcı, M., 2020. The aetiology of the neotectonic evolution of Turkey. Mediterr. Geosci. Rev. 2, 327–339.
Sheather, S.J., Jones, M.C., 1991. A Reliable Data-based Bandwidth selection Method for Kernel Density Estimation. J. R. Stat. Soc. Ser. B 53, 683–690.
Stein, R.S., Toda, S., Özbakir, A.D., Sevilgen, V., Gonzalez-Huizar, H., Lotto, G., Sevilgen, S.. Interactions, Stress Changes, Mysteries, and Partial Forecasts of the 2023 Kahramanmaraş, Türkiye, Earthquakes, Temblor. http://doi.org/10.32858/temblor.299.
Stiros, S.C., 2022. Earthquakes, tsunamis, dried harbours and seismic coastal uplift: evidence from the Eastern Mediterranean. Mediterr. Geosci. Rev. 4, 319–328. https://doi.org/10.1007/s42990-022-00079-8.
Stucchi, M., Sesetyan, K., Augusto Antonio, G.C., Sbeinati, M.R., 2022. Exploiting the legacy of N.N. Ambraseys: known and unknown earthquakes in the Anatolian area. Mediterr. Geosci. Rev. 4, 555–568. https://doi.org/10.1007/s42990-022-00087-8.
Sümer, Ö., Drahor, M., Ongar, A., Tepe, C., Duman, A., 2023. 2023. 06 SUBAT 2023, Mw=7.7 Pazarcık, Mw=7.6 Elbistan (Kahramanmaraş) ve 20 SUBAT 2023, Mw=6.4 Defne (Hatay) depremleri saha çalişmalari yerbilimsel ön raporu 1 (In Turkish), p. 66.
Taftsoglou, M., Valkaniotis, S., Papathanassiou, G., Karantanellis, E., 2023. Satellite imagery for rapid detection of liquefaction surface manifestations: the case study of Türkiye–Syria 2023 earthquakes. Remote Sens. 15, 4190. https://doi.org/10.3390/rs15174190.
Tan, O., Tapirdamaz, M.C., Yörük, A., 2008. The earthquake catalogues for Turkey. Turk. J. Earth Sci. 17, 405–418.
Tanyaş, H., Lombardo, L., 2019. Variation in landslide-affected area under the control of ground motion and topography. Eng. Geol. 260 https://doi.org/10.1016/j.enggeo.2019.105229.
Tanyaş, H., van Westen, C.J., Allstadt, K.E., Anna Nowicki Jessee, M., Görüm, T., Jibson, R.W., Godt, J.W., Sato, H.P., Schmitt, R.G., Marc, O., Hovius, N., 2017. Presentation and analysis of a worldwide database of earthquake-induced landslide inventories. Case Rep. Med. 122 https://doi.org/10.1002/2017JF004236.
Tanyaş, H., Kirschbaum, D., Lombardo, L., 2021. Capturing the footprints of ground motion in the spatial distribution of rainfall-induced landslides. Bull. Eng. Geol. Environ. https://doi.org/10.1007/s10064-021-02238-x.
Tanyaş, H., Hill, K., Mahoney, L., Fadel, I., Lombardo, L., 2022. The world's second-largest, recorded landslide event: Lessons learnt from the landslides triggered during and after the 2018 Mw 7.5 Papua New Guinea earthquake. Eng. Geol. 297, 106504 https://doi.org/10.1016/j.enggeo.2021.106504.
Tatar, O., Sözbilir, H., Koçbulut, F., Bozkurt, E., Aksoy, E., Eski, S., Özmen, B., Alan, H., Metin, Y., 2020. Surface deformations of 24 January 2020 Sivrice (Elazığ)–Doğanyol (Malatya) earthquake (Mw = 6.8) along the Pütürge segment of the East Anatolian Fault Zone and its comparison with Turkey's 100-year-surface ruptures. Mediterr. Geosci. Rev. 2, 385–410. https://doi.org/10.1007/s42990-020-00037-2.
Taymaz, T., Eyidogan, H., Jackson, J., 1991. Source parameters of large earthquakes in the East Anatolian Fault Zone (Turkey). Geophys. J. Int. 106, 537–550. https://doi.org/10.1111/j.1365-246X.1991.tb06328.x.
Taymaz, T., Ganas, A., Yolsal-Çevikbilen, S., Vera, F., Eken, T., Erman, C., Keleş, D., Kapetanidis, V., Valkaniotis, S., Karasante, I., Tsironi, V., Gaebler, P., Melgar, D., Öcalan, T., 2021. Source mechanism and rupture process of the 24 January 2020 Mw 6.7 Doğanyol–Sivrice earthquake obtained from seismological waveform analysis and space geodetic observations on the East Anatolian Fault Zone (Turkey). Tectonophysics 804, 228745. https://doi.org/10.1016/j.tecto.2021.228745.
Tian, Y., Owen, L., Xu, C., Shen, L., Zhou, Q., Figueiredo, P., 2020. Geomorphometry and Statistical analyses of Landslides Triggered by the 2015 Mw 7.8 Gorkha Earthquake and the Mw 7.3 Aftershock, Nepal. Front. Earth Sci. https://doi.org/10.3389/feart.2020.572449.
U.S. Geological Survey, 2023a. M 7.5 - Elbistan earthquake, Kahramanmaras earthquake sequence, USGS Earthquake Hazards Program. [WWW Document]. URL. https://earthquake.usgs.gov/earthquakes/eventpage/us6000jlqa (accessed 5.15.23).
U.S. Geological Survey, 2023b. M 7.8 - Pazarcik earthquake, Kahramanmaras earthquake sequence, USGS Earthquake Hazards Program. [WWW Document]. URL. https://earthquake.usgs.gov/earthquakes/eventpage/us6000jllz (accessed 5.15.23).
Wald, D., Quitoriano, V., Thompson, E., Goldberg, D., Xu, S., Noh, H., 2023. U.S. In: Geological Survey's Hazard and Impact Assessment of the 2023 Türkiye Earthquake Sequence, in: SSA Annual Meeting 2023, Puerto Rico.
Westaway, R., 2003. Kinematics of the Middle East and eastern Mediterranean updated. Turk. J. Earth Sci. 12, 5–46.
Xu, C., Xu, X., Yao, X., Dai, F., 2014. Three (nearly) complete inventories of landslides triggered by the May 12, 2008 Wenchuan Mw 7.9 earthquake of China and their spatial distribution statistical analysis. Landslides 11, 441–461. https://doi.org/10.1007/s10346-013-0404-6.
Zhao, B., 2021. Landslides triggered by the 2018 Mw 7.5 Palu supershear earthquake in Indonesia. Eng. Geol. 294, 106406 https://doi.org/10.1016/j.enggeo.2021.106406.